

Journal of Geophysical Research: Solid Earth**RESEARCH ARTICLE**

10.1002/2016JB013007

Key Points:

- Time variable regularization only derived from GRACE information without any model information
- Global solutions from GRACE to be used without postprocessing
- High-resolution equal area 1 degree global mascon solutions from GRACE

Correspondence to:

H. Save,
save@csr.utexas.edu

Citation:

Save, H., S. Bettadpur, and B. D. Tapley (2016), High resolution CSR GRACE RL05 mascons, *J. Geophys. Res. Solid Earth*, 121, 7547–7569, doi:10.1002/2016JB013007.

Received 13 MAR 2016

Accepted 16 SEP 2016

Accepted article online 23 SEP 2016

Published online 10 OCT 2016

High-resolution CSR GRACE RL05 mascons**Himanshu Save¹, Srinivas Bettadpur¹, and Byron D. Tapley¹**¹Center for Space Research, The University of Texas at Austin, Austin, Texas, USA

Abstract The determination of the gravity model for the Gravity Recovery and Climate Experiment (GRACE) is susceptible to modeling errors, measurement noise, and observability issues. The ill-posed GRACE estimation problem causes the unconstrained GRACE RL05 solutions to have north-south stripes. We discuss the development of global equal area mascon solutions to improve the GRACE gravity information for the study of Earth surface processes. These regularized mascon solutions are developed with a 1° resolution using Tikhonov regularization in a geodesic grid domain. These solutions are derived from GRACE information only, and no external model or data is used to inform the constraints. The regularization matrix is time variable and will not bias or attenuate future regional signals to some past statistics from GRACE or other models. The resulting Center for Space Research (CSR) mascon solutions have no stripe errors and capture all the signals observed by GRACE within the measurement noise level. The solutions are not tailored for specific applications and are global in nature. This study discusses the solution approach and compares the resulting solutions with postprocessed results from the RL05 spherical harmonic solutions and other global mascon solutions for studies of Arctic ice sheet processes, ocean bottom pressure variation, and land surface total water storage change. This suite of comparisons leads to the conclusion that the mascon solutions presented here are an enhanced representation of the RL05 GRACE solutions and provide accurate surface-based gridded information that can be used without further processing.

1. Introduction

The Gravity Recovery and Climate Experiment (GRACE) mission was launched in March 2002 under the NASA Earth System Science Pathfinder Program. GRACE is jointly implemented by the U.S. National Aeronautics and Space Administration (NASA) and German Aerospace Center. The twin GRACE satellites were launched into near polar orbits with an along-track separation of approximately 200 km at an altitude of 500 km. The primary instrument on the GRACE satellites is the K-Band Ranging system (KBR) that measures the intersatellite range to a precision of a few microns. This is the fundamental measurement for the GRACE gravity recovery. Using these precise KBR measurements along with other measurements like global positioning system (GPS), attitude control system, and accelerometer measurements, the average monthly global gravity field is estimated in the form of Stokes' coefficients (C_{lm} and S_{lm}) which are provided as the official gravity products by the GRACE project. The GRACE mission has been instrumental in providing valuable measurements of the long-term mean component and the time-variable component of the mass distribution in the Earth's system [Tapley *et al.*, 2004b, 2004c]. Over the past decade, the mass flux estimates obtained from GRACE have significantly improved our understanding of the Earth's system including the ground water distribution, polar ice, and ocean dynamics [Chambers, 2006; Rodell *et al.*, 2004; Velicogna, 2009; Famiglietti *et al.*, 2011; Long *et al.*, 2013; Scanlon *et al.*, 2015; Luthcke *et al.*, 2013].

GRACE mass flux and distribution has been traditionally estimated from the changes in the Earth's gravitational potential which is typically represented by spherical harmonic expansion [Tapley *et al.*, 2004a]. The effect of high-degree harmonic coefficients on the satellite's orbit is small as compared to the low-degree harmonic coefficients. As the altitude increases, there is a faster attenuation of the contribution of high-degree harmonics to the Earth's potential as compared to low-degree harmonics. In the presence of modeling and instrument errors and due to weaker observability in the east-west direction, the estimates of the high-degree harmonic coefficients have increased errors in the estimation procedure for the Stokes' coefficients [Tapley *et al.*, 2004a]. Because of these modeling and instrument errors in combination with the ill-posed inverse problem, the anomaly maps obtained from the unconstrained GRACE spherical harmonic solutions show physically unrealistic north-south stripes. These errors have typically been mitigated by applying a destriping

filter [Swenson and Wahr, 2006], filtering using empirical orthogonal functions [Schrama and Wouters, 2011], Gaussian smoothing [Wahr et al., 1998], Wiener optimal filtering [Sasgen et al., 2012], etc., as postprocessing. These postprocessing methods have a tendency to attenuate the real geophysical signals [Landerer and Swenson, 2012]. Lemoine et al. [2007], Mayer-Gürr [2007], Bruinsma et al. [2010], etc., have applied some combination of constraint and truncation to stabilize the problem. Save et al. [2012] have used Tikhonov regularization with variable regularization matrix and regularization parameter to significantly reduce the stripe errors in the GRACE time-variable spherical harmonic solutions and demonstrated that their regularized spherical harmonic solutions captured all the signal within the GRACE noise levels.

In addition to spherical harmonics, the other common basis functions used to estimate mass flux from GRACE is the use of mass concentration (mascon) blocks. Groups at Jet Propulsion Laboratory (JPL) [Watkins et al., 2015], Goddard Space Flight Center (GSFC) [Rowlands et al., 2010; Luthcke et al., 2006, 2013], etc., have developed GRACE mascon solutions for various applications. The mascon solutions developed in this study have three key elements. (1) The regularization is purely derived from GRACE information only and no external model or data is used to inform the constraints. (2) The regularization matrix is time variable and will not bias or attenuate future regional signals based on past statistics from GRACE or other models. (3) The mascon solutions are estimated on a geodesic grid of the size equivalent to equatorial 1°.

A mascon solution approach estimates the mass anomalies at specified mass concentration blocks or grid location. There are typically three different mascon approaches used. Watkins et al. [2015] used explicit partial derivatives with analytical expression for mass concentration to relate the intersatellite range-rate measurements to the individual mascons. In the second approach, the mascons are related to the range-rate or the range-acceleration data via a spherical harmonic expansion that is truncated at a finite degree and order as demonstrated by the group at GSFC [Luthcke et al., 2006, 2008; Sabaka et al., 2010; Rowlands et al., 2010; Luthcke et al., 2013]. In the third approach, the mascons are fit to the spherical harmonic coefficients obtained from GRACE. This method is essentially a form of postprocessing since the process of computing mass anomaly estimates has no direct knowledge of the observation range-rate data from GRACE. The examples of this form of postprocessing is demonstrated by Jacob et al. [2012]; Velicogna et al. [2014]; Schrama et al. [2014] in their analysis of the GRACE data.

We implement the second type of mass flux estimation problem where we define each mass tile as a finite truncated spherical harmonic representation up to degree and order 120 which are in turn related to the range-rate observation via their partial derivatives (section 3). While we need $n = 179$ to represent 1° equiangular grid, this procedure uses geodesic grid that is roughly 1° at the equator or 120 km wide. Moreover, the choice of using $n = 120$ truncation for partial derivatives was made in order to keep the computational requirements manageable during experimentation. The next generation of these mascon solutions will use $n = 180$ truncated partial derivatives to avoid any inherent error in the mascon solutions due this choice of truncation of the partial derivatives.

We distribute the Earth's mass on a geodesic grid, which is a collection of hexagonal (and 12 pentagonal) tiles distributed over the Earth's surface to fit against each other. The size of each tile is approximately 1° equatorial longitudinal distance. The formulation of this geodesic grid is described in section 2. The mass anomaly for each of the mass tile is estimated using the KBR range-rate observations and the associated spherical harmonic partial derivatives. The singular estimation process is stabilized using Tikhonov regularization [Save et al., 2012] with a time-variable regularization matrix. The Center for Space Research (CSR) mascon solutions, like JPL mascons [Watkins et al., 2015] and GSFC mascons [Luthcke et al., 2013], are global and can be used for all applications such as hydrology, oceanography, and the cryosphere without any postprocessing and/or filtering and without applying any empirical scaling factors.

2. Geodesic Grid

A geodesic grid is a technique used to model the surface of a sphere (such as the Earth) with a subdivided polyhedron, usually an icosahedron. For our purpose, it is a global Earth reference that uses cells or tiles to statistically represent data encoded to the area covered by the cell location and is different from the conventional equiangular latitude-longitude based grid. We use a geodesic grid to represent estimates of the mass anomalies over the Earth surface. This choice is made mainly to ensure homogeneity and isotropy since the resulting tiles are approximately equal area and minimally distorted. The geodesic grid, like any high-resolution spatial grid, also allows us to resolve the scales of the regions of interest and delineate the coastlines and basins

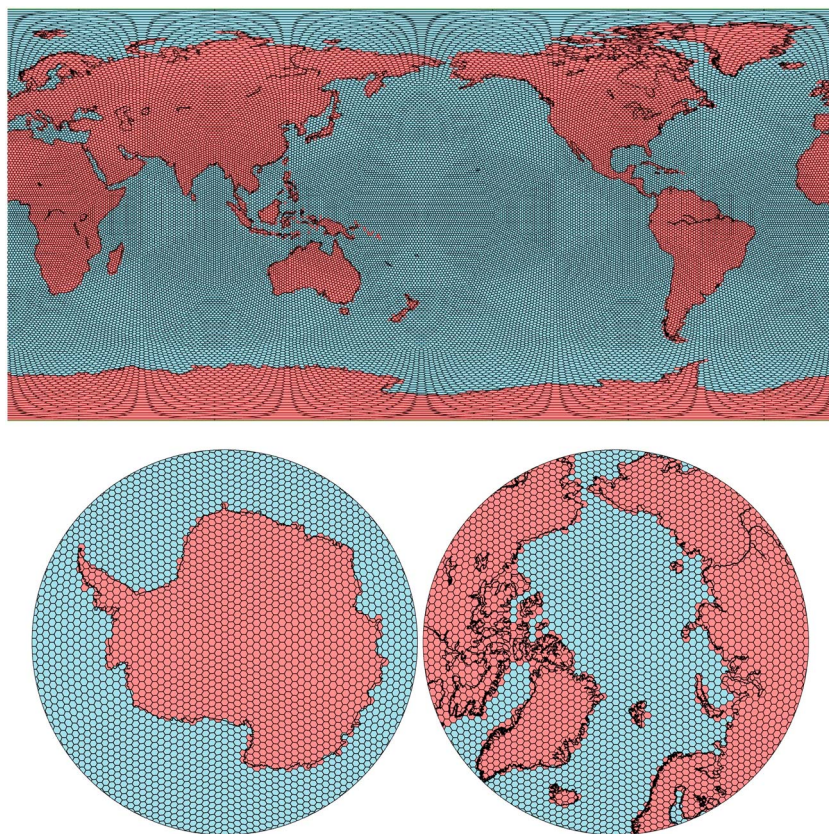


Figure 1. The distribution of 40,962 geodesic grid tiles over the Earth used as a basis function for estimation of mass anomalies from GRACE for CSR mascon solutions. (top) Global view, (bottom left) South Pole view, and (bottom right) North Pole view.

accurately. It does not suffer from oversampling near the poles, and unlike an equiangular grid, there is no single point of contact between neighboring cells. The one downside of using a geodesic grid is the complexity of implementation as compared to a simple equiangular latitude-longitude-based grid. A geodesic grid is generated with a set of nearly evenly spaced points on a sphere [Ringler and Randall, 2002]. The use of a sphere as a basis to define the geodesic grid is similar to the use of sphere in the development spherical harmonic coefficients and in the spherical cap mascons used by JPL. The estimated global mascons have a C_{20} component that accounts for the oblateness. Moreover, in the final analysis of these solutions the C_{20} component is replaced by the satellite laser ranging (SLR) derived C_{20} and will minimize any errors related to this assumption.

We start with a regular icosahedron circumscribed by a unit sphere and then bisect each face into four new equal triangles. The new vertices are then projected onto the unit sphere resulting in a polyhedron with high number of vertices. We repeat this process until we have a polyhedron with 40,962 vertices. Each vertex is assumed to be the center of a tile/cell. There are a total of 40,950 hexagonal tiles and 12 pentagonal tiles. The original 12 vertices of the regular icosahedrons are the centers of the pentagonal tiles, and new subdivided vertices are the centers of the hexagonal tiles. There are about 320 cells along the equator, and the size of each cell is about 1° equatorial longitudinal distance. The average area of each cell is approximately $12,400 \text{ km}^2$ with the average distance of approximately 120 km between the cells. The geodesic grid shown in Figure 1 is the basis for this study. The geodesic grid was generated using a variation of the code published by Laven [2010].

3. Mascon Inversion

The mascon parameters or the geodesic tile elements are used to estimate the global mass correction to the a priori mean background model. The variability of mass in each tile is expressed as centimeter of equivalent water height represented as a uniform mass layer of water. In this analysis we follow the mascon formulation

described by *Rowlands et al.* [2010]. The development starts with equations to compute the gravity potential at the satellite altitude using Stokes' coefficients [*Tapley et al.*, 2004a].

$$U(r, \vartheta, \lambda) \approx \frac{GM}{R} \left[\sum_{l=0}^{l_{\max}} \sum_{m=0}^l \left(\frac{R}{r} \right)^{l+1} \bar{P}_{lm}(\sin \vartheta) (\bar{C}_{lm} \cos(m\lambda) + \bar{S}_{lm} \sin(m\lambda)) \right] \quad (1)$$

where, ϑ is the latitude, λ is the longitude, and r is the spherical geocentric radius of the point where the geopotential is evaluated; M is the Earth's mass; G is the universal gravitational constant, R is the mean radius of the Earth; l and m represent the spherical harmonic degree and order; \bar{C}_{lm} and \bar{S}_{lm} are the fully normalized Stokes' coefficients, and \bar{P}_{lm} represent the fully normalized associated Legendre functions. *Rowlands et al.* [2010] describe the computation of the change in potential coefficients ($\Delta \bar{C}_{ilm}(t)$ and $\Delta \bar{S}_{ilm}(t)$) caused due to the addition of a small uniform layer of mass over a region, which is a geodesic tile (j) in this study.

$$\begin{aligned} \Delta \bar{C}_{ilm}(t) &= \frac{\sigma_j(t) (1 + k'_j) R^2}{M(2l + 1)} \int \bar{P}_{lm}(\sin \vartheta) \cos m\lambda d\Omega \\ \Delta \bar{S}_{ilm}(t) &= \frac{\sigma_j(t) (1 + k'_j) R^2}{M(2l + 1)} \int \bar{P}_{lm}(\sin \vartheta) \sin m\lambda d\Omega \end{aligned} \quad (2)$$

where the integrals are evaluated over the geodesic tile j . The loading Love number of degree l is represented by k'_j to account for the Earth's elastic yielding; $\sigma_j(t)$ represents the mass of the layer over the geodesic tile, j , at the epoch t ; and Ω is the surface area of the geodesic tile, j , in a solid angle representation. The units of $\sigma_j(t)$ are Kg/m^2 which is evaluated as $10.25 \times h_j(t)$, where 1025 kg/m^3 is the density of water and $h_j(t)$ represents the height of a uniform layer of water in the region, j , expressed in centimeters. $h_j(t)$ is the parameter we estimate by relating the differential potential equations to the observation equations. The time tag t associated with each parameter is the time tag of the estimate which in this study is the mean over an approximately 30 day time span. Since we do not apply any time correlations in this study each estimation problem relates to a specific time tag, and so we drop the time tag, t from all the subsequent equations. We can rewrite the equation (2) in terms of the estimated parameter, h_j as follows,

$$\begin{aligned} \Delta \bar{C}_{ilm} &= h_j \left[\frac{10.25 (1 + k'_j) R^2}{M(2l + 1)} \right] \int \bar{P}_{lm}(\sin \vartheta) \cos m\lambda d\Omega \\ \Delta \bar{S}_{ilm} &= h_j \left[\frac{10.25 (1 + k'_j) R^2}{M(2l + 1)} \right] \int \bar{P}_{lm}(\sin \vartheta) \sin m\lambda d\Omega \end{aligned} \quad (3)$$

We subdivide the surface of the earth into equal area geodesic tiles to a granularity of about 120 km at which point we approximate the integral over the geodesic tile j in the above equation with a finite summation where $\bar{P}_{lm}(\sin \vartheta) \cos m\lambda$ is evaluated at the center of the geodesic tile and $d\Omega$ is approximated to the area A_j of the geodesic tile, j . We assume that the error associated with this approximation is very small and ignore it. These assumptions leads to the following:

$$\begin{aligned} \Delta \bar{C}_{ilm} &= \left[\frac{10.25 (1 + k'_j) R^2}{M(2l + 1)} \right] h_j A_j \bar{P}_{lm}(\sin \vartheta_j) \cos m\lambda_j \\ \Delta \bar{S}_{ilm} &= \left[\frac{10.25 (1 + k'_j) R^2}{M(2l + 1)} \right] h_j A_j \bar{P}_{lm}(\sin \vartheta_j) \sin m\lambda_j \end{aligned} \quad (4)$$

where ϑ_j is the geocentric latitude of the center of j th tile and λ is the geocentric longitude of the center of j th tile. The equation (4) approximates the change in the geopotential coefficients due to surplus (or deficit) of a uniform layer of water of height h_j over the geodesic tile j . Hence, the total change in the geopotential coefficients, $\Delta \bar{C}_{lm}$ and $\Delta \bar{S}_{lm}$, due to the change in the mass in each of the 40,962 geodesic tile regions can be computed as a summation of each of the $\Delta \bar{C}_{ilm}$ and $\Delta \bar{S}_{ilm}$, respectively.

$$\begin{aligned} \Delta \bar{C}_{lm} &= \left[\frac{10.25 (1 + k'_j) R^2}{M(2l + 1)} \right] \sum_{j=1}^{40962} h_j (\bar{P}_{lm}(\sin \vartheta_j) \cos m\lambda_j) A_j \\ \Delta \bar{S}_{lm} &= \left[\frac{10.25 (1 + k'_j) R^2}{M(2l + 1)} \right] \sum_{j=1}^{40962} h_j (\bar{P}_{lm}(\sin \vartheta_j) \sin m\lambda_j) A_j \end{aligned} \quad (5)$$

GRACE processing for spherical harmonic solutions at CSR employs orthogonal transformations *Tapley et al.* [2004a] to convert the design matrix or the information matrix H of size $m \times n$ in the least squares estimation process to an upper triangular matrix R of size $n \times n$.

$$Rx = b \quad (6)$$

where $QH = R$ and $Qy = b$ and Q is the orthogonal matrix that transforms the H matrix to R matrix that is upper triangular and the observations y to a corresponding b vector. The \hat{x} vector is made up of all the global spherical harmonic coefficients truncated to n_{\max} , which in this study is $n_{\max} = 120$. The reader is encouraged to refer to *Tapley et al.* [2004a] and *Save* [2009] for the details on this procedure and how it is implemented at CSR for the GRACE processing. During the processing of the GRACE data, the upper triangular R matrices are saved on the disc which are used in this study for computation of the GRACE mascon solutions. The choice of using the $R|b$ system instead of $H|y$ system reduces the problem size and computational resources significantly in this study.

Once we define our vector x consisting of all the spherical harmonic coefficients ($\Delta C_{lm}/\Delta S_{lm}$) and a vector z of size 40,962 as our new state vector consisting of the equivalent water height, h_j , for each of the $j = 40,962$ geodesic tiles, equations (5) can be expressed as

$$x = Tz \quad (7)$$

where x is a vector of all the $\Delta C_{lm}/\Delta S_{lm}$ and T is the transformation matrix that transforms the mass anomaly in the units of centimeters of equivalent water in each geodesic tile to the change in the spherical harmonic coefficients. If $T(a, j)$ is the entry in the transformation matrix T at the a th row and j th column and if $x(a)$ entry in vector x is C_{lm} , then

$$T(a, j) = \left[\frac{10.25 (1 + k'_l) R^2}{M(2l + 1)} \right] (\bar{P}_{lm}(\sin \vartheta_j) \cos m\lambda_j) A_j \quad (8)$$

where A_j is area of the j th tile. Similarly, if $x(a)$ is S_{lm} then

$$T(a, j) = \left[\frac{10.25 (1 + k'_l) R^2}{M(2l + 1)} \right] (\bar{P}_{lm}(\sin \vartheta_j) \sin m\lambda_j) A_j \quad (9)$$

The equations (8) and (9) help populate the transformation matrix T in equation (7). Substituting equation (7) into equation (6) and defining $RT = \bar{H}$, we get the following equation (10)

$$\bar{H}z = b \quad (10)$$

Equation (10) gives us a transformed linear system of equations that relate the satellite range-rate observations to the mass anomalies in each of the geodesic tiles to be estimated. This system of equations is rank deficient. We start with the R matrices that are constructed during the estimation of the spherical harmonic RL05 solutions and transform these matrices from the spherical harmonic domain into the spatial (z) domain using the transformation T . We apply the Tikhonov regularization techniques using L-ribbon approach described in *Save et al.* [2012] to stabilize these rank-deficient system of equations given by equation (10). By defining an invertible matrix (M) of size $j \times j$, called the regularization matrix, and a scalar (μ), called the regularization parameter, we formulate the Tikhonov regularization problem to estimate the new state vector (z) using the following equation.

$$\hat{z} = (\bar{H}^T \bar{H} + \mu M^T M)^{-1} \bar{H}^T b \quad (11)$$

where $\bar{H} = RT$.

Save et al. [2012] provide more detailed development and implementation of the Tikhonov regularization approach as it relates to the GRACE estimation problem. We define the regularization matrix, M , and discuss its development in section 4. The scalar μ is evaluated using the L-ribbon approach as discussed in *Save et al.* [2012].

4. Regularization Matrix

Previous studies [*Watkins et al.*, 2015; *Rowlands et al.*, 2010] have used geophysical models to constrain their mascon solutions. Using geophysical models to constrain the mascon solutions can introduce regional errors

in the gridded mascon solutions if the geophysical models used to develop the constraints are not adequate in that region. If the regularization is not too tight, these regional errors in the mascon solutions due to the error in constraints can be mitigated but may introduce stripe errors in the solutions due to very loose regularization. In addition, using a fixed constraint for the entire GRACE mission may not be consistent with the temporal variability captured by the GRACE measurements. This issue is considered in the next section (section 5) which discusses the influence of the constraints on the GRACE data and the mascon solutions.

In this section we develop the constraint, or regularization matrix (M), from only the information contained in the GRACE measurements. We do not use any geophysical models to inform the development of the regularization matrix. Also, we develop a regularization matrix that is time variable and represents the geophysical properties for the particular data measurement interval while retaining the long-term geophysical characteristics of the signals from GRACE.

The regularization matrix is designed as a two-step process. Step 1 is used to develop intermediate GRACE solutions that have significantly less leakage of land signals into the ocean as compared to grids obtained from the regularized spherical harmonic solutions. Step 2 then uses these intermediate solutions to design the time-variable regularization matrices for estimating the mascon solutions. This two-step process allows us to develop time-variable regularization that is purely based on GRACE information while preventing the signal leakage into the ocean.

4.1. Design of the Regularization Matrix—Step 1

Save et al. [2012] developed regularized spherical harmonic solutions from GRACE that had significantly reduced striping errors while capturing all the signal within the noise level of GRACE. The new versions of regularized spherical harmonic GRACE solutions developed from and after that study became the fundamental information that was used to develop the mascon solutions in this study. These regularized spherical harmonic solutions were based on an approach in which only the error estimate from the RL05 monthly spherical harmonic solutions was used to constrain the error in these solutions. The regularization matrices for the mascon solutions in this study were developed in two steps starting from the regularized spherical harmonic solutions.

The first step was used to isolate the land signal information within the land boundaries and reduce the leakage into the ocean. A global RMS grid of the signal was computed from the regularized spherical harmonic solutions from April 2002 to November 2014, as shown in Figure 2a. This RMS grid has leakage into the ocean from the land especially for the large ice signals. We also see slight leakage of the hydrology signals into the oceans, but these signals are well contained within the land boundaries for the most part. In addition, there is high RMS up to 10–14 cm in the regions with earthquake signals and in the regions around Gulf of Carpentaria, Siberian Sea, Baltic sea, etc. In order to prevent leakage from the ice signals into the ocean while allowing for the freedom in the regularization for the earthquake signals and the GRACE signals in these closed seas, the RMS over the ocean was set at a uniform 4 cm except for the regions where the RMS is greater than 4 cm. We do this while making sure that the geodesic tiles near the coast of Antarctica, Greenland, Alaska, and other ice-loss related signals do not have RMS values greater than 4 cm. The high RMS in the geodesic tiles over the regions of the earthquake signals and the signals in the closed seas as seen in Figure 2a were retained in this grid. For the RMS over the land, all the RMS values less than 4 cm were fixed to 4 cm while retaining all the values greater than 4 cm as computed from the regularized spherical harmonic solutions. The resulting grid, shown in Figure 2b, is adopted as the inverse of regularization matrix (M^{-1}) for the first step. Using equation (11) and estimating the regularization parameter with the L-ribbon approach outlined in *Save et al.* [2012], we estimated the mascon parameters defined by the z vector, the equivalent water height of mass anomaly in each of the 40,962 geodesic tiles, for each of monthly solution from April 2002 to May 2014. This set of mascon solutions is referred to as the intermediate mascon solutions and becomes the starting point for Step 2.

4.2. Design of the Regularization Matrix—Step 2

The intermediate mascon solutions have little or no leakage of the land signals into the ocean but may have stripe errors or some signal attenuation. This is acceptable since the first step is to reduce or eliminate the leakage of the land signals into the oceans. These intermediate solutions then provide the information required to define the final regularization matrix (M). The amplitude of the signals in different regions of the globe vary over ± 300 cm—from the ice loss signals at the high latitudes to the high-variability annual signals over the tropical regions. Regional solutions with such large signal amplitude have the potential for large errors and require regularization parameters to accommodate this possibility. Overconstrained solutions lead to a signal

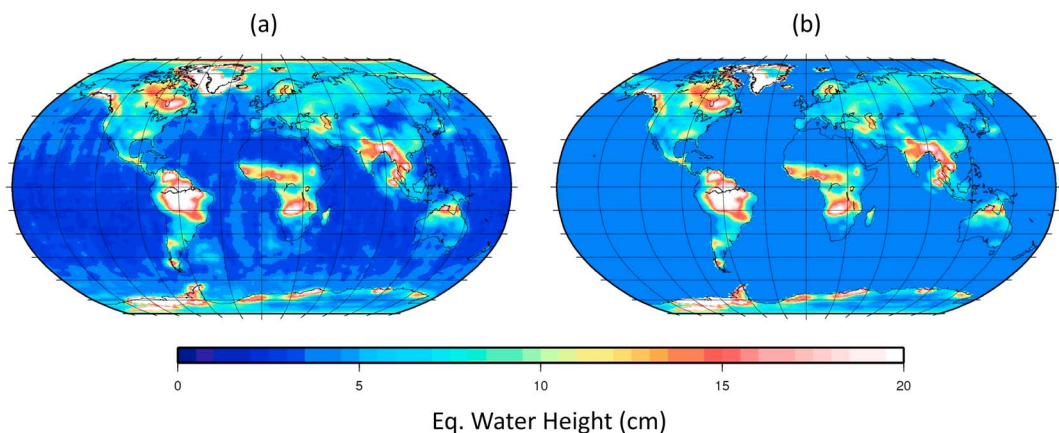


Figure 2. (a) RMS grid of the variability of the regularized GRACE spherical harmonic solutions from CSR [Save et al., 2012]. This grid is the starting point for the development of the regularization matrix in this study. (b) Grid representation of the regularization matrix used for step 1 in section 4.1. This grid is engineered from the grid shown on Figure 2a to prevent the leakage of land signals into the ocean.

peak reduction, while underconstrained solutions have large errors in the mascon estimates resulting in error stripe effect in the overall solution. In some regions the signal is dominated by decadal trends and annual variations. One way to prevent overconstraint during regularization is by forward modeling the large annual and trend signals in the solution and estimating only the corrections to the forward model when applying the regularization. The final result is then the combination of forward model signals and the corrections from regularized GRACE estimates.

A secular trend and a periodic annual signal is fit to the intermediate grid time series obtained in Step 1. The interannual variability in the hydrology signals associated with droughts and floods usually shows up as secular signals in the fits. We did not want to bias the resulting mascon solutions to the secular trends in the hydrology signals in the forward model from the intermediate mascon solutions. The primary reason to forward model the secular trend is to account for the large trends in the GRACE observations that are not associated with hydrology before determining the mascon solutions. Hence, the forward model was designed such that only the secular trend grid associated with ice loss signals, glacial isostatic adjustment (GIA) trend, and the global annual grid were used to compute the forward model. Experiments performed by Save and Bettadpur [2013] suggested that the C_{21} signal in the mascon solutions in the intermediate grid showed signal attenuation in its secular trend. Hence, the secular trend and annual fit estimate of C_{20} and C_{21} from RL05 GRACE unconstrained spherical harmonic solutions was used to replace these values in the forward model, as a grid, in order to prevent signal attenuation of the C_{21} secular signal. We achieve this by applying some corrections to the linear trend and annual fits computed for the intermediate solutions obtained in Step 1 as follows:

1. For linear trend component of the forward model (say, L_{FM}): We use the linear trend from the intermediate solutions obtained in Step 1 (let us refer to it as L_{S1}). From this we remove the C_{20} and C_{21} linear trend obtained from Step 1 (say L_{C20}^{S1} and L_{C21}^{S1} , respectively). Then the ICE5G GIA model (say, L_{GIA}) as described by Geruo et al. [2013] is subtracted. From the resulting grid, only the linear trend values greater than 2 cm/yr for latitude $\geq 50^\circ$ and latitude $\leq -45^\circ$, and in the regions right around the Sumatra and Fukushima earthquakes are retained and the all the other grid values are set to 0. Let us call this high-latitude ice and earthquake filter (HLIEF) for this discussion. The linear trend grids of the C_{20} and C_{21} estimates from GRACE RL05 spherical harmonic solutions (say, L_{C20}^{RL05} and L_{C21}^{RL05} , respectively) are then added along with the GIA trend grid (L_{GIA}) that was subtracted to give us the desired linear trend component for our forward model (L_{FM}). Hence,

$$L_{FM} = \text{HLIEF} [L_{S1} - L_{C20}^{S1} - L_{C21}^{S1} - L_{GIA}] + L_{C20}^{RL05} + L_{C21}^{RL05} + L_{GIA} \quad (12)$$

The result of these steps is that (1) trend estimate of C_{20} and C_{21} from RL05 spherical harmonic solutions is used in the forward model and (2) only GRACE trend estimates for signals related to ice loss from Step 1

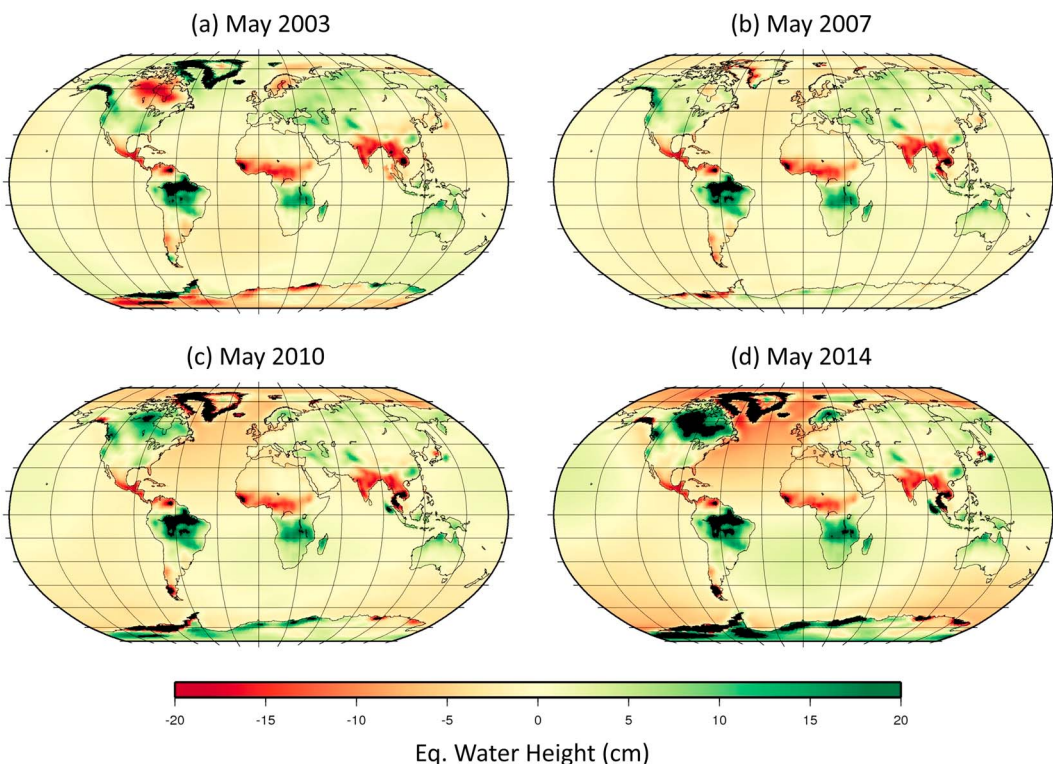


Figure 3. Map representation of the forward modeled grid used to estimate the mascon solutions. (a) May 2003, (b) May 2007, (c) May 2010, and (d) May 2014. Note the absence of the secular hydrology signals in these forward modeled grids.

- are retained in the forward model. (3) Sumatra and Fukushima earthquake signals get forward modeled as trends. (4) Hydrology-related trends are not included in the forward model.
2. For annual component of the forward model (say, A_{FM}): We use the annual fit from the intermediate solutions obtained in Step 1 (say A_{S1}). From this we remove the C_{20} annual component associated with step1 (A_{C20}^{S1}) and add the annual component of C_{20} computed from RL05 spherical harmonic solutions (A_{C20}^{RL05}) to give us the desired annual component of the forward model (A_{FM}).
- Hence,

$$A_{FM} = A_{S1} - A_{C20}^{S1} + A_{C20}^{RL05} \quad (13)$$

The resulting combination of the linear and annual forward model is that only the high-latitude ice loss signals, GIA, and earthquake signals are forward modeled as trend and annual component is forward modeled for all regions. While this process uses remove/restore of GIA signal, there is a dependence on the ICE5G GIA model by Geruo *et al.* [2013] for the forward model used. We assume that some of the error in the GIA forward model will be corrected by GRACE during the mascon estimation process. The sample forward modeled signal for May 2003, May 2007, May 2010, and May 2014 is shown in Figure 3. One should note that these forward model grid maps do not show the secular signals observed by GRACE in the hydrology regions. Residuals of the intermediate mascon solutions with respect to the forward modeled signals were computed for each solution. The 12 distinct monthly RMS values (January RMS, February RMS, etc.) of this residual became the basis for the regularization matrix in this study. Let us refer to this grid as $G1(t)$ —a long-term GRACE mission statistic where t refers to a GRACE solution span.

4.3. Time Variable Regularization Matrix

We wanted to ensure that the long-term statistics of the RMS of this residual does not adversely influence recovery of the monthly signals in the mascon. For instance, if there is no hydrological or meteorological drought signal in a given region observed by GRACE and if this region experiences a severe drought or flood in the future, then the long-term statistics computed for the observed interval and used for the regularization matrix will attenuate the future drought or flood signals in that region. This sensitivity analysis is discussed in the following section (section 5).

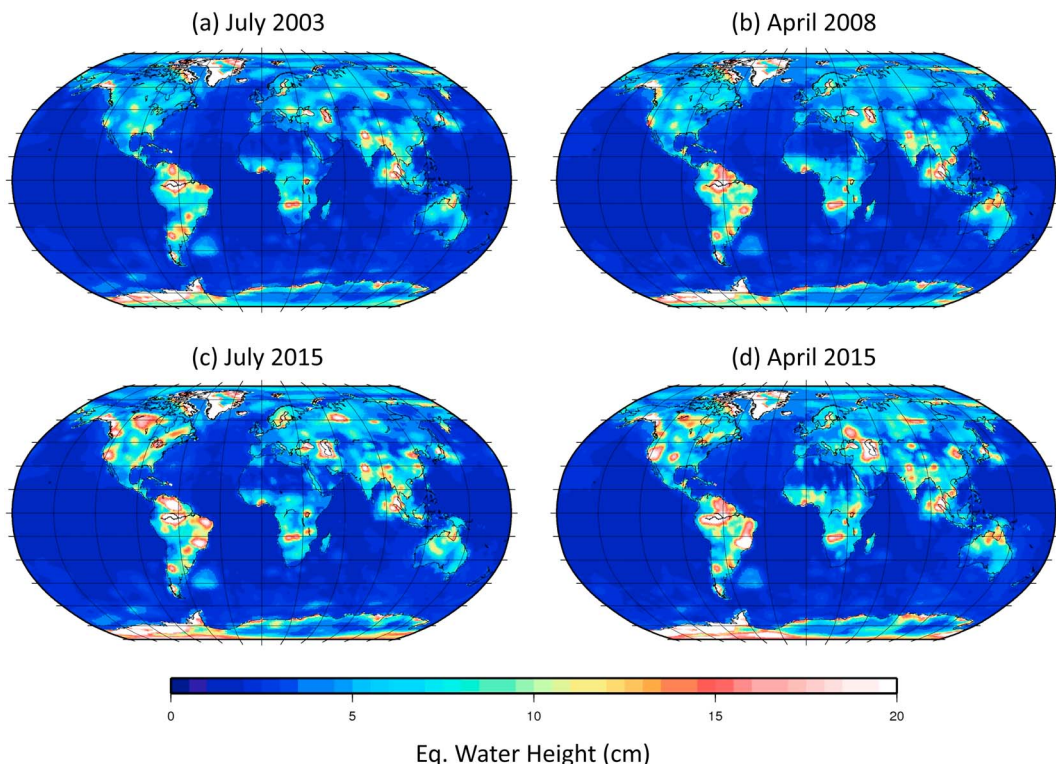


Figure 4. Time variable regularization matrices as applied for the regularization and inversion of the mascon solutions. (a) July 2003, (b) April 2008, (c) July 2015, and (d) April 2015. Note the difference in the regularization matrices even for the same months in different years.

In order to make the system immune to this sensitivity we have developed a time-variable regularization matrix that is informed by the long-term statistics, grid $G1(t)$, described above, as well as the monthly signal information from the specific GRACE monthly solution. For every monthly solution we compute a regularized spherical harmonic solution as described in *Save et al. [2012]*. We then apply a 200 km Gaussian smoothing and compute the residual with respect to the forward model for that solution as described in section 4.2. This residual approximates the expected smoothed signal that the regularization should be applied to. Let us refer to this residual grid at time tag t as $G2(t)$. Then, for every monthly solution, the final regularization matrix is designed as follows:

For $j = 1, 40, 962$ at any given time step t (solution span),

$$\begin{aligned} M^{-1}(j, t) &= \text{Max}[G1(j, t), G2(j, t)] \quad \text{for land tiles} \\ M^{-1}(j, t) &= \quad G1(j, t) \quad \quad \quad \text{for ocean tiles} \end{aligned} \quad (14)$$

where, $M^{-1}(j, t)$ is the diagonal entry in the M^{-1} matrix at the j th row and j th column for the solution at time t . Because the 200 km smoothing applied in computation of $G2(t)$ has leakage from land into the ocean, we only use the information from $G1(t)$ over the ocean in order to prevent the leakage of the land signals into the ocean in the final mascon solutions. The off-diagonal entries in the M^{-1} matrix are zero. The time-variable regularization matrix is hence purely derived from GRACE data with no model information or independent data information used to define the regularization matrix. The example time-variable regularization matrices represented as grids are shown in Figure 4. Note the differences in the regularization matrices for same calendar month for different years.

The studies performed by *Watkins et al. [2015]* and *Rowlands et al. [2010]* specified correlations between neighboring cells in their constraint matrix. In our extensive tests we found that applying correlations degrade our resulting mascon solutions. We observe that applying the correlations led to solutions which show significantly more longitudinal stripes than the solutions without the correlations. The tests also showed that our 3° global mascon solutions are less susceptible to stripes due to the correlations applied, but our 1° global mascon solutions developed in this study show stripes when applying the correlations. The other benefit of not

applying the correlations is the significant reduction in the computational resources. Because of these factors, this study does not allow correlations between neighboring cells and the resulting regularization matrix is diagonal.

5. Sensitivity to Regularization Matrix

Save *et al.* [2012] had discussed the need for time variable regularization when computing the regularized spherical harmonic solutions. Using the same philosophy, it is important to demonstrate the sensitivity of the GRACE solutions to fixed and time-variable constraints. There are several key questions that need to be addressed when designing the regularization. What is the best information to use to design the constraint? If we use model statistics to design the constraint, how will that impact the signals estimated by the system? If we use GRACE statistics from a certain time to design the constraints, how will that impact the signals estimated during that time period and how will that impact the signals estimated during the time period not included in the statistics? In order to answer some of these questions and to understand the sensitivity of the regularized mascon solutions to the design of the regularization matrix, we designed an experiment. This experiment will use three regularizations designed as follows:

1. The regularization matrix is designed in section 4, referred to as RC (release candidate).
2. A fixed regularization matrix is designed with the residuals described in section 4.2 but only using the residuals from 2004 to 2009 to form the elements of the regularization matrix. This regularization matrix does not have information about the floods or droughts that occurred before 2004 or after 2009. We refer to this regularization case as 0409F.
3. Starting from the fixed regularization matrix designed above (0409F), we apply the time variable information from the monthly GRACE spherical harmonic solution as described in equation (14). This regularization is referred to as 0409V.

This experiment will test whether or not the fixed regularization, designed using statistics from a certain time period, can capture extreme signals outside that time period. If not, can we add a time-variable component to the fixed regularization that will capture those extreme signals?

We computed the mascon solutions for the entire mission with each of these three regularization matrices. Analysis show that most of the basin average times series around the globe were largely insensitive to the three different types of regularizations. But there are several basins, especially the ones that had seen exceptional droughts and floods before 2004 or after 2009, that were sensitive to this experiment. A few examples are shown in Figure 5. In the example of Lake Eyre river basin we see that the 0409F case attenuates the flood signal captured by GRACE in early 2011. But adding the time variable component by using 0409V regularization captures the entire flood signal as seen in the release candidate solutions (RC). Similarly, the 0409F regularization case attenuates the 2010 flood signals in High Plains North region, the 2010 flood signal in Wisla Vistula river basin, and the 2002–2003 and 2015 flood signals in Dulce river basin. The time variable variation case (0409V) of the fixed regularization cases (0409F) is able to capture correct estimates of these flood signals as seen in the release candidate solutions, even though the statistic used to design the regularization matrix for 0409V was derived from 2004 to 2009 time span. Because of the sensitivity of these mascon solutions to the regularization applied, we have chosen to apply a time variable regularization in this study as described in the section 4.3. This ensures that the CSR mascon solutions will not attenuate the GRACE signals due to departures in the nominal behavior of the regional signals and the regularization will always be able to capture significant departures in the nominal behavior of the regional signals.

6. Solution Analysis

In this section we evaluate the mascon solutions computed in this study. We perform regional and global comparison with the results from the spherical harmonic RL05 solutions from CSR postprocessed at GRACE Tellus [Swenson, 2012; Swenson and Wahr, 2006; Landerer and Swenson, 2012; Chambers, 2012; Chambers and Bonin, 2012; Chambers and Willis, 2010], RL05.1M version Mascon solutions from JPL [Wiese, 2015; Watkins *et al.*, 2015], and other models like Global Land Data Assimilation System (GLDAS) hydrological model [Rodell *et al.*, 2004] and Estimating the Circulation and Climate of the Ocean (ECCO) ocean bottom pressure model [Fukumori, 2002; Kim *et al.*, 2007] and in situ ocean bottom pressure recorder data [Macrander *et al.*, 2010]. In order to maintain consistency and compatibility of the signal definition of these solutions with other GRACE

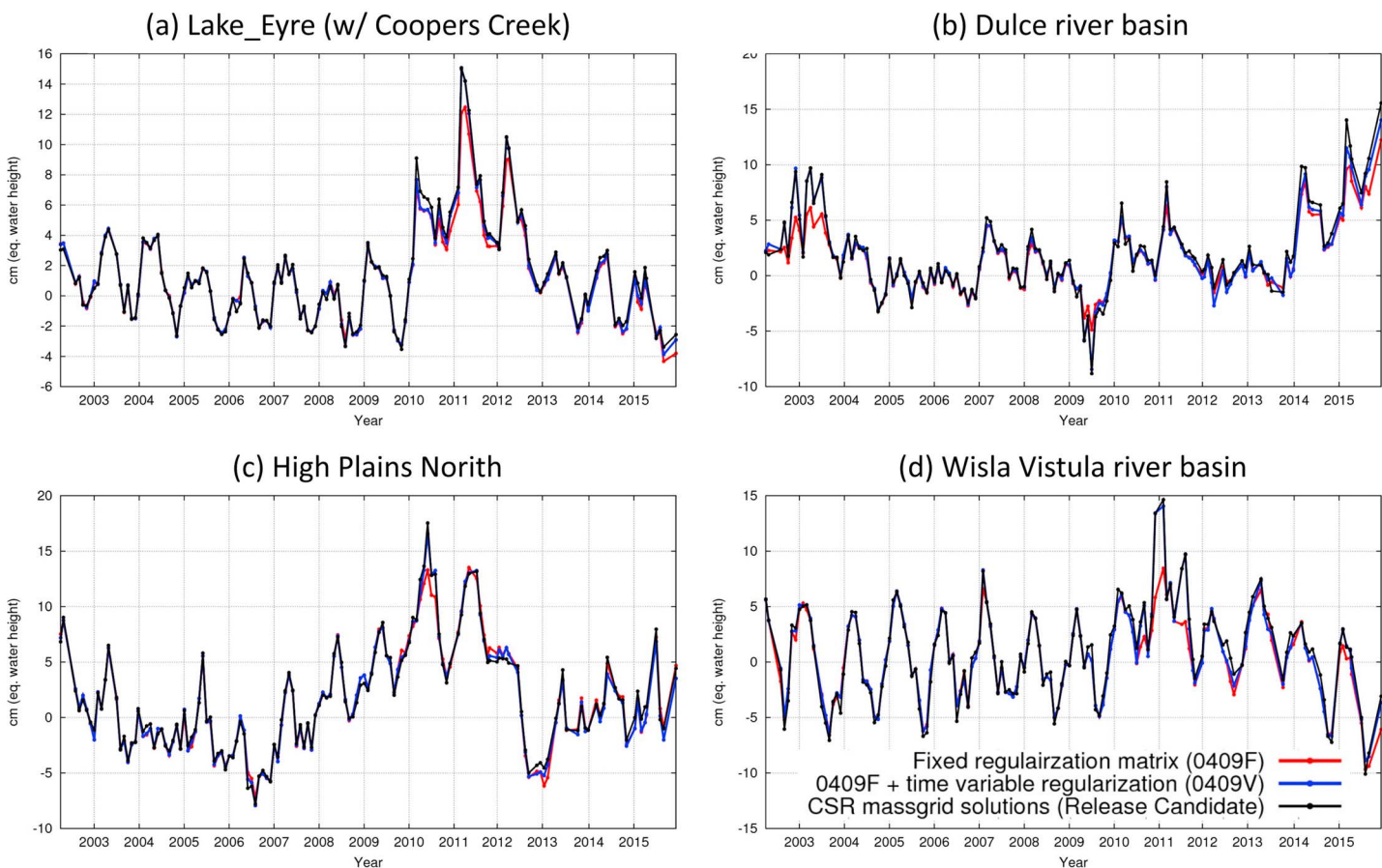


Figure 5. Semiarid regions show high sensitivity to the regularization matrix. The time variable regularization applied using the RC and 0409V show higher amplitudes in these regions especially after 2011 as compared to the cases that use 0409F regularization matrix. (a) Lake Eyre basin, (b) Dulce river basin, (c) High Plains Aquifer North region, and (d) Wisla Vistula river basin. Note the attenuation of the signals during floods when using the fixed regularization case (0409F). The time variable case (0409V) is able to capture the flood signals.

products, we have applied certain corrections as used in the products provided by GRACE Tellus. We have replaced the C_{20} coefficients with those provided by *Cheng and Tapley* [2004]. We have corrected the mass grids with the degree 1 contribution as computed by *Swenson et al.* [2008]. These mascon solutions have also been corrected for the glacial isostatic adjustment (GIA) signals using *Geruo et al.* [2013]. The mascon solutions computed in this study are resynthesized as spherical harmonic coefficients for evaluation in the degree spectrum.

6.1. Degree Variance Scatter

Figure 6 shows the comparison of the power as degree variance scatter of different solutions with respect to the respective population mean. The different solutions used in this comparison are (1) the CSR mascon solutions, (2) CSR unconstrained RL05 solutions, (3) postprocessed version of CSR solutions from Tellus (land grids [*Swenson, 2012*] + ocean grids [*Chambers, 2012*]), and 4) a model combination of GLDAS [*Rodell et al., 2004*] and ECCO ocean bottom pressure [*Fukumori, 2002; Kim et al., 2007*]. We combine the Tellus land and Tellus ocean grids in order to have a uniform signal definition for all compared products. We combine the GLDAS and ECCO fields for the same reason. We see from the Figure 6 that the low-degree signal in the mascon solutions is identical to the unconstrained RL05 solutions until about degree 14 where the two solutions deviate. This is roughly the degree where the errors in GRACE start dominating the signal amplitude [*Save et al., 2012*]. This shows that the CSR mascon solutions capture all of the low-degree time-variable signals. The decreasing energy of the mascon solutions with increasing degree agrees with the behavior of the geophysical models [*Wahr et al., 1998*]. This is also seen in degree spectrum of the models (GLDAS+ECCO) in Figure 6. The land + ocean grids from Tellus have significantly lower power at all degrees past degree 10 as compared to the

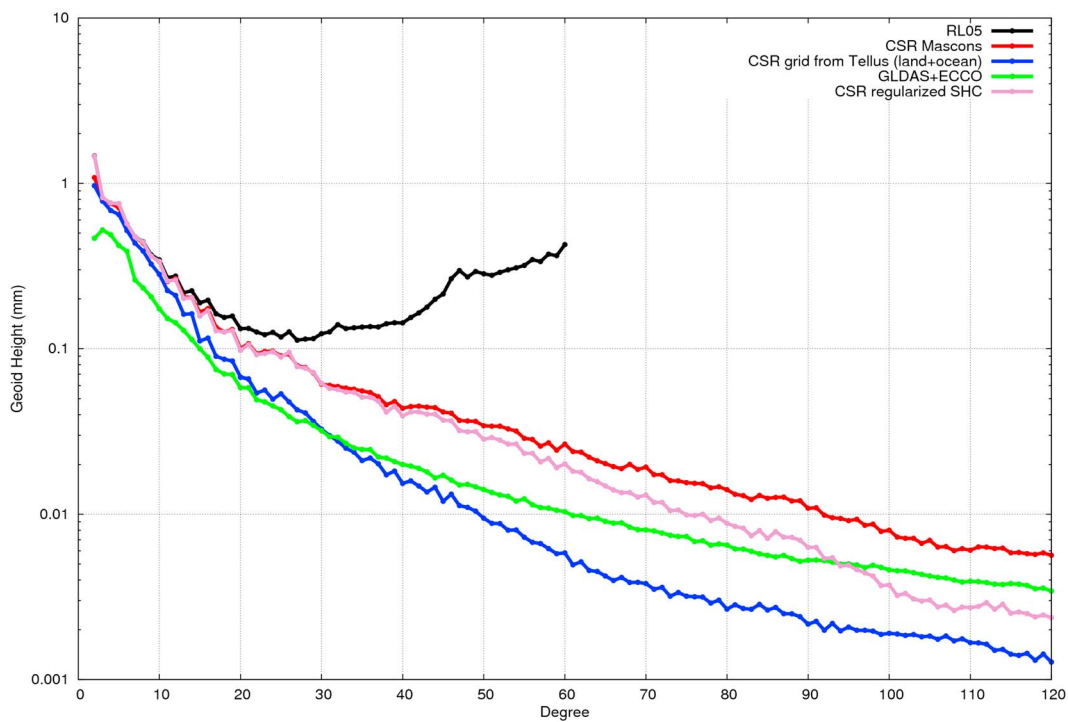


Figure 6. Degree variance scatter with respect to the population mean. CSR Mascon solution captures all the low-degree signals in RL05 unconstrained solutions and has significantly higher amplitude across the entire spectrum as compared to the Tellus land + ocean grids or the models. The plot also shows the degree variance of the CSR-regularized spherical harmonic solutions used to design the regularization matrix for the CSR mascon solutions.

CSR mascon solutions, and the CSR mascon solutions consistently have higher power at all wavelengths than the model (GLDAS + ECCO) signal. These observations for CSR mascon solutions are consistent with those observed by *Watkins et al.* [2015] for JPL mascon solutions.

6.2. Trend Maps and Annual Amplitude Maps

We compare the global trends and annual amplitudes of the CSR mascon solutions with the land grids processed at Tellus and the mascon solutions from JPL. We choose the JPL mascon solutions and Tellus provided grids as representative solutions for comparison. The choice of using JPL mascon solutions was made in order to compare with a representative solution from GRACE Science Data System (SDS) center. Figures 7–10 compare the trends computed over the U.S., South America, Asia, and globally, respectively. The trend patterns from the three GRACE products are similar in most of the regions. Also apparent is that the signal amplitude over drought regions of California [*Famiglietti et al.*, 2011], south central United States [*Long et al.*, 2013; *Scanlon et al.*, 2015], and ground water depletion signals over Indian subcontinent [*Rodell et al.*, 2009; *Tiwari et al.*, 2009] is significantly higher in the mascon solutions from JPL and CSR as compared to the postprocessed grids from Tellus. We also observe that the signals in the CSR mascon solutions show higher apparent resolution and have gradual change along adjacent 1° mascons as compared to the sharp step change seen between adjacent 3° mascons in the JPL mascon solutions. The oceans are zeroed out in these images to compare with the gridded Tellus land product that does not provide the data over the oceans. The leakage of the land signals or lack thereof can be seen in the global ocean bottom pressure images in Figures 14 and 13, which do not show any land signal leaked into the ocean near the coast of Greenland and Antarctica.

Figure 11 is the annual amplitude for the three solution cases—CSR mascons, Tellus land grids, and JPL mascons. It shows a general agreement in patterns between the three solution cases, but Figure 11 also shows the higher amplitude in the CSR and JPL mascon solutions. A closer investigation reveals higher apparent resolution and gradual change along adjacent 1° mascons in CSR solutions as compared to the sharp step changes between the adjacent 3° mascons in the JPL mascon solutions as seen in the regional trend maps.

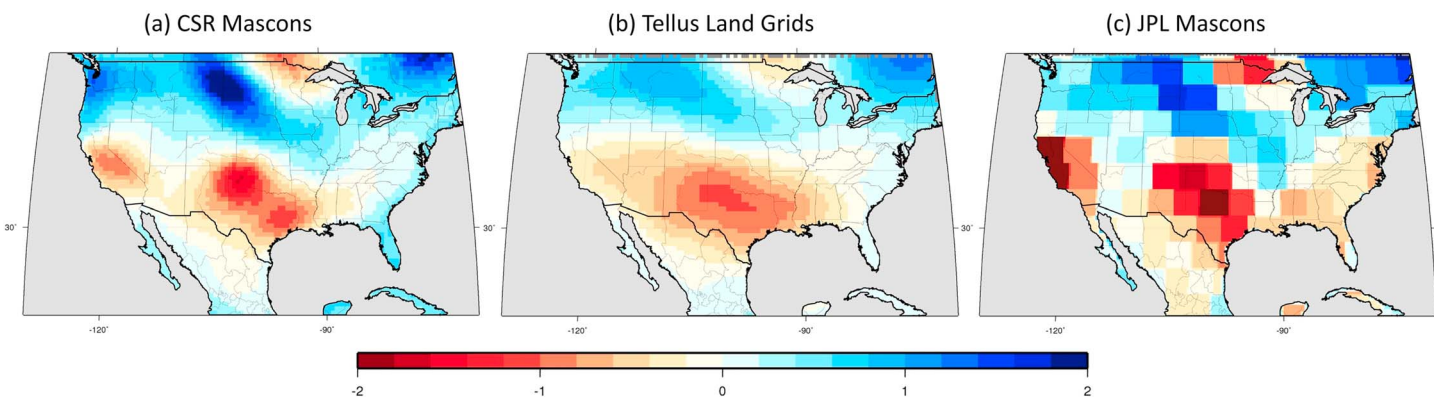


Figure 7. GRACE trends over continental United States. (a) CSR Mascon solutions, (b) Tellus land grids, and (c) JPL Mascon solutions. The postprocessed grids from Tellus smears all the signals due to destriping and smoothing. CSR mascons show gradual change along adjacent 1° mascons as compared to the sharp step changes between the adjacent 3° mascons in the JPL mascon solutions.

6.3. Analysis of the Postfit Residual

We compute the postfit residuals by fitting the observation data to the solutions and computing $(y - H\hat{x})$ for every observation $y(t)$. The parametrization and the solution fail to capture a part of the observation that is discarded as postfit residuals. As described by Save *et al.* [2012], a differentiating low-pass CRN filter [Thomas, 1999] is applied to the postfits and are analyzed locally in range acceleration domain. We chose to use range-acceleration domain because it localizes the signal better than in the range-rate domain. A map of these range-acceleration residuals show how well the data fits the solutions. If there is a signal attenuation due to postprocessing or due to application of constraints, then these residuals will contain the part of the signal that was attenuated or constrained in the observation domain. Such a map will show

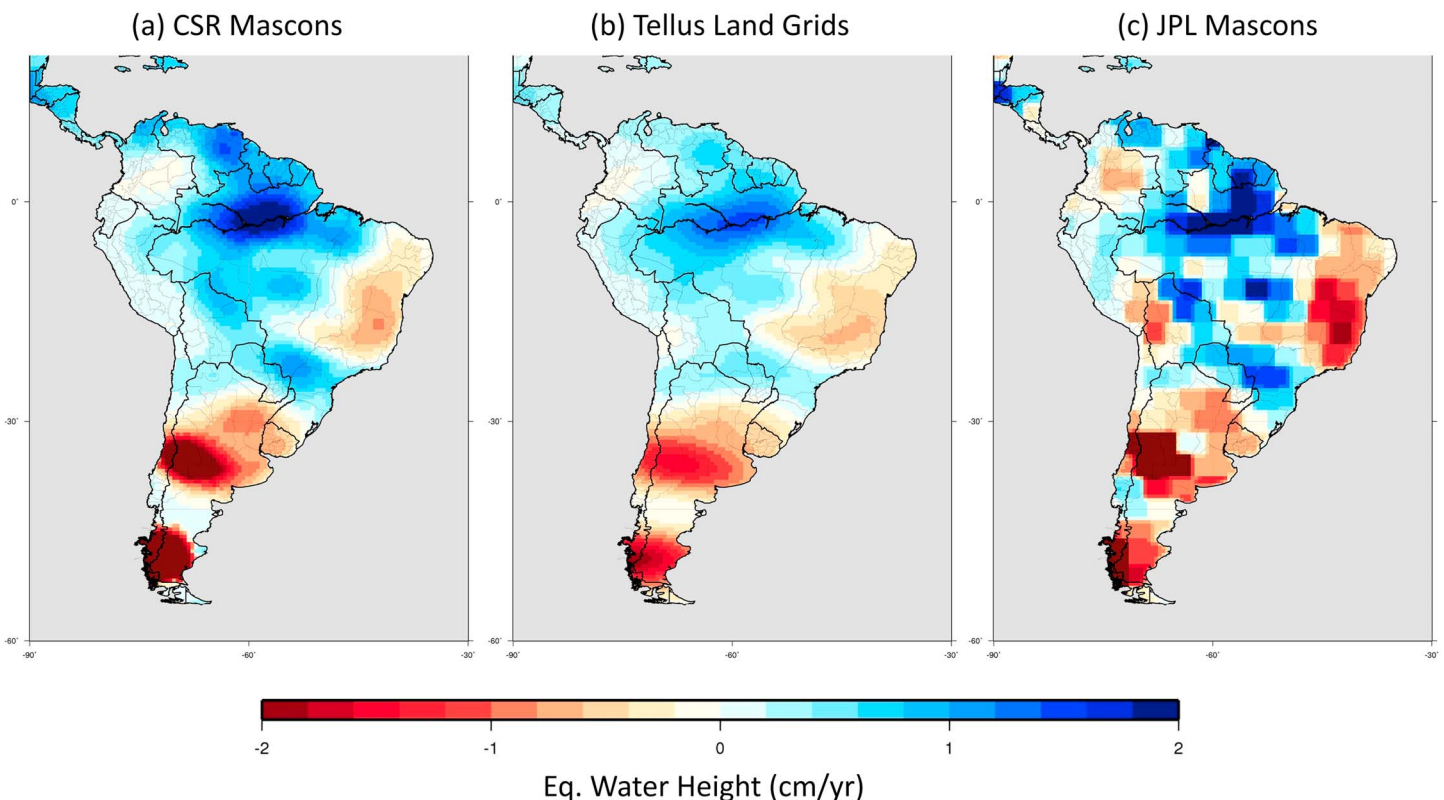


Figure 8. GRACE trends over South America. (a) CSR Mascon solutions, (b) Tellus land grids, and (c) JPL Mascon solutions. The postprocessed grids from Tellus smears all the signals due to destriping and smoothing. CSR mascons show gradual change along adjacent 1° mascons as compared to the sharp step changes between the adjacent 3° mascons in the JPL mascon solutions.

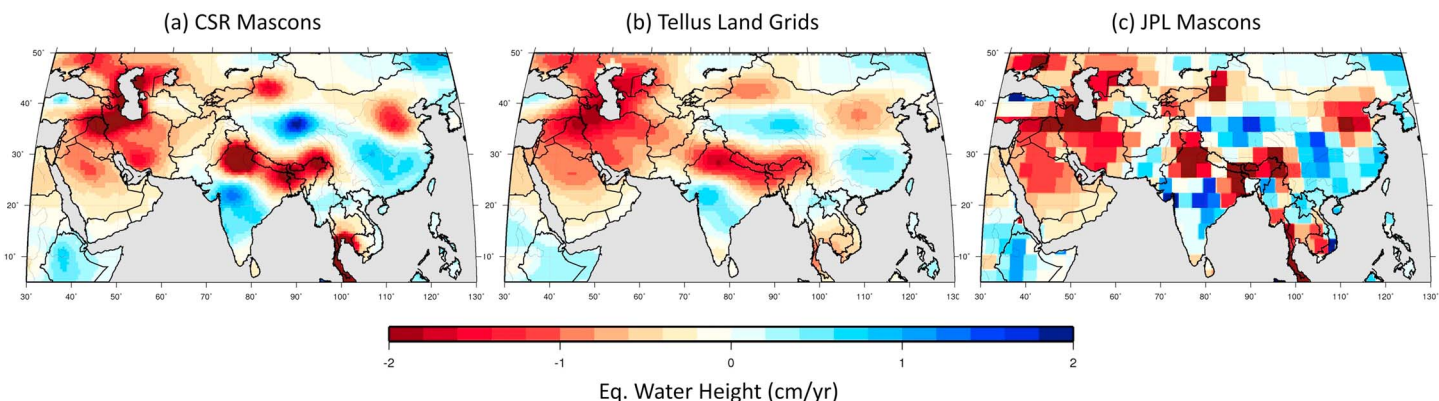


Figure 9. GRACE trends over Asia. (a) CSR Mascon solutions, (b) Tellus land grids, and (c) JPL Mascon solutions. The postprocessed grids from Tellus smears all the signals due to destriping and smoothing. CSR mascons show gradual change along adjacent 1° mascons as compared to the sharp step changes between the adjacent 3° mascons in the JPL mascon solutions.

geospatially correlated range-acceleration signals corresponding to the signal attenuation. Hence, postfit analysis is a necessary condition to make sure that the solutions capture all the geophysical signals as described by the observation data.

Postfit analysis is only a necessary condition and not sufficient. We need to perform other analysis to test for sufficiency that all the data inverted into the solutions have been localized correctly. This is analogous to the fact that if GRACE observes a point mass at a location then the inverted gravity field solution will observe the point mass as a “blob” due to the band-limited nature of the GRACE observations. But the postfit analysis will meet the necessary condition that all the observed signal is described by this gravity field. But the sufficiency of this gravity field will depend on the required resolution of the solution (point mass or a 400 km mass anomaly blob).

We perform a postfit residual test with every solution we generate to ensure that the solution has met the necessary condition. Figure 12 shows the RMS of the postfit residuals on the left and the RMS of the prefit residuals (O-C) on the right. Prefit residuals is the full observation signal in the range-acceleration domain that is inverted into the gravity field. We observe that the map of the postfit residuals show no geospatially correlated signal with the maximum value of 2.05 nm/s^2 which is smaller than the GRACE errors of about 4 nm/s^2 [Save et al., 2012]. While a mission long statistic map is shown in Figure 12, this observation is true for monthly analysis as well. We thus claim that all the observed signals have been captured by the mascon solutions hence meeting the necessary condition.

The L-ribbon approach outlined in Save et al. [2012] gives an optimal parameter μ as described in the paper and any potential overdampening of signal due to regularization is checked by performing a postfit residual

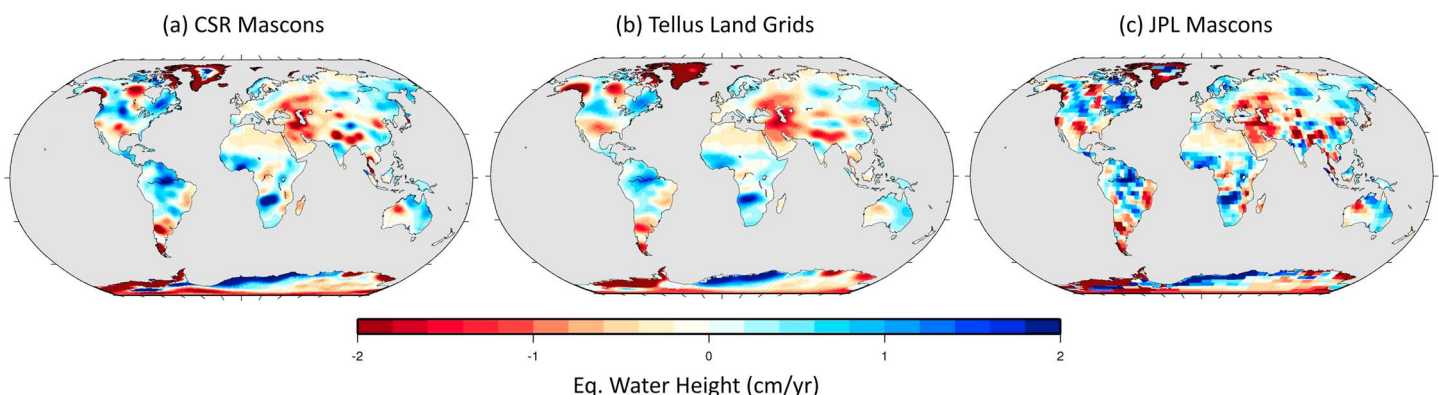


Figure 10. Global trends from GRACE. (a) CSR mascon solutions, (b) Tellus land grids, and (c) JPL mascon solutions. The postprocessed grids from Tellus smears all the signals due to destriping and smoothing. CSR mascons show gradual change along adjacent 1° mascons as compared to the sharp step changes between the adjacent 3° mascons in the JPL mascon solutions.

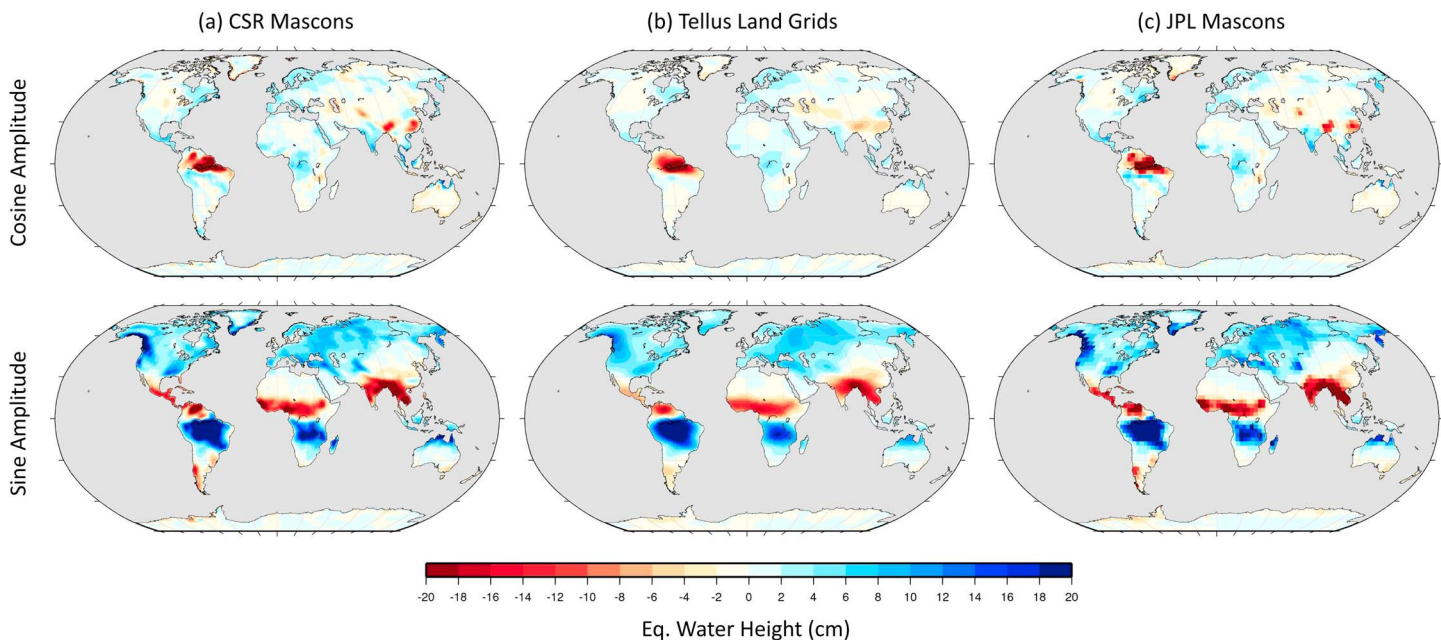


Figure 11. Cosine and sine annual amplitudes. (a) CSR Mascon solutions, (b) Tellus land grids, (c) JPL Mascon solutions. The postprocessed grids from Tellus smears all the signals due to destriping and smoothing. CSR mascons show gradual change along adjacent 1° mascons as compared to the sharp step changes between the adjacent 3° mascons in the JPL mascon solutions.

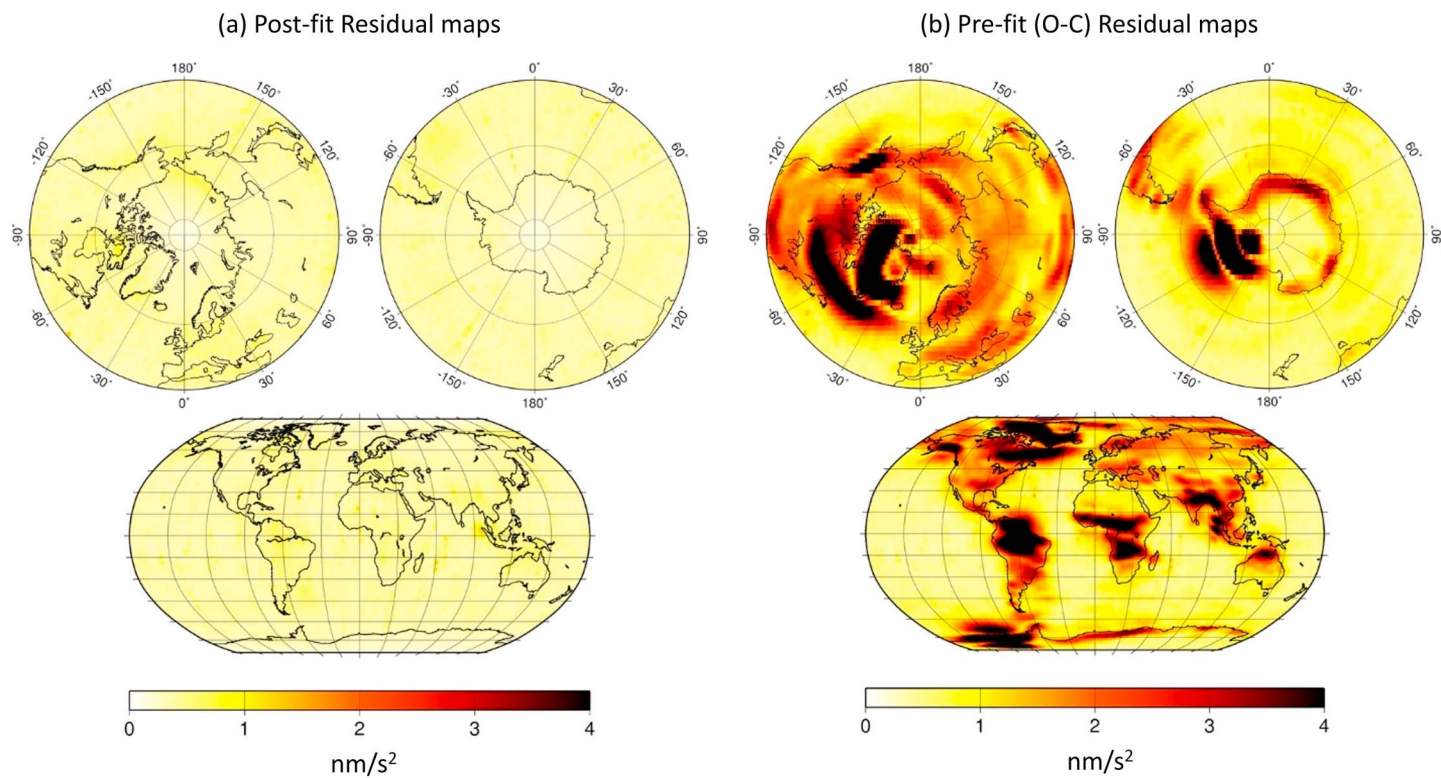


Figure 12. (a) RMS of the postfit residuals after fitting the CSR mascon solutions to the GRACE range-rate observation data (maximum value = 2.05 nm/s^2). (b) RMS of the prefit O-C or the size of the full signal inverted into mascon solutions (maximum value = 24.5 nm/s^2). Note the absence of geophysical correlation in the postfit maps (left). The CSR mascon solution satisfies the necessary condition and captures all the signal within the noise level of GRACE.

analysis as described here. We do not see geophysically correlated postfit residuals within the noise level of GRACE, which is our convergence criteria. Any solution that shows evidence of signal dampening is corrected by manually tuning the μ value to err on the side of caution by allowing in more noise to enter the solution while eliminating over dampening of the signals. We believe that iterating constrained solutions has a potential to bake in errors or signal dampening made in the earlier iterations if the regularization is not left sufficiently free. We chose to not iterate our solutions but try to capture all the signal within the noise level of GRACE in one pass of the data.

6.4. Oceans

We perform qualitative and quantitative assessment of the CSR mascon solutions in comparison with the ocean grids obtained from Tellus [Chambers, 2012; Chambers and Bonin, 2012; Chambers and Willis, 2010] and the mascon solutions from JPL [Wiese, 2015; Watkins et al., 2015]. We compare the total ocean bottom pressure maps from the three solutions as a qualitative analysis and then compare the solutions with the in situ ocean bottom pressure recorder data [Macrander et al., 2010] in a correlation analysis.

6.4.1. Standard Deviation Over the Ocean

Figure 13 shows the maps of the standard deviation over the ocean for CSR mascon solutions, Tellus ocean grid (a product widely used by the science community), and the JPL mascon solutions [Wiese, 2015; Watkins et al., 2015]. The loss of resolution and amplitude attenuation is evident in the Tellus ocean grids as compared to the CSR mascon solutions and the JPL mascon solutions. Also evident is the ice-loss signals leaking into the oceans due to postprocessing near Greenland and Antarctica in the Tellus Ocean grids. The CSR mascon solutions show signals in the Arctic Ocean which are not seen in the Tellus ocean grids. Also evident in the maps is the 1° resolution of the CSR mascon solutions as compared to the 3° resolution of the JPL mascon solutions.

Figure 14 shows the standard deviation of the total ocean bottom pressure seen by CSR GRACE mascon solutions (a), the Ocean Model for Circulation and Tides (OMCT) [Flechtnar, 2007] model used as a de-aliasing product for GRACE processing (b), and the corrections to OMCT applied by the GRACE observations (c). The CSR mascon solutions correct the OMCT model in the Arctic Ocean, Southern Ocean, along the Argentine gyre, and the closed seas at a significantly higher resolution than seen before from GRACE.

6.4.2. Comparison With Ocean Bottom Pressure Recorder Data

Several studies have demonstrated that the oceanic signals observed by GRACE are equivalent to the signals observed by the ocean bottom pressure recorders [Peralta-Ferriz et al., 2014; Macrander et al., 2010; Kanzow et al., 2005; Böning et al., 2008]. Macrander et al. [2010] generated a database of all available ocean bottom pressure records coincident with GRACE time span. Watkins et al. [2015] used these ocean bottom pressure recorder data to validate JPL mascon solutions over the ocean. We chose to use the same technique to validate CSR mascon solutions. Carmen Boening provided access to the ocean bottom pressure (OBP) recorder database for this study where all data were quality controlled. Watkins et al. [2015] provide a brief discussion on how the recorder data were corrected for errors, outliers, and drifts.

We selected 28 ocean bottom pressure data records from the database with more than 18 months of data without monthly data gaps. These were grouped into five groups (South Atlantic, tropical Atlantic, North Atlantic near Svalbard, Arctic, and Kuroshio Extension in northwest Pacific) as shown in Figure 15. We calculate the correlation between the in situ OBP data time series with CSR Mascons, JPL Mascons, Ocean grid from Tellus and OMCT model which is used as de-aliasing background model for GRACE processing.

The mascon solutions both from JPL and CSR show higher correlation with all the ocean bottom pressure data as compared to the Tellus Ocean fields which are derived from destriped and smoothed spherical harmonic solutions (Figure 16). In South Atlantic (Group A), the CSR mascon solutions perform statistically slightly better than the JPL mascon solutions except for three recorders. For all the recorders in the South Atlantic region we observe that the mascon solutions significantly improve over the background OMCT model with average improvement of 0.5 in correlation. In the tropical Atlantic (Group B) while the correlation of the CSR mascon time series with OBP record is around 0.5, it significantly improves over the OMCT background model which has a correlation of 0.1. It should also be noted that the Tellus Ocean grid time series shows significant negative correlation possibly due to the leakage of the hydrological signal from the nearby Amazon basin. Until the recent developments in the quality and resolution of the state-of-the-art global mascon solutions, it has been challenging to capture oceanic signals with weak barotropic dynamics and low-amplitude especially in the presence of leakage from the nearby hydrology basins like the Amazon river basin [Watkins et al., 2015].

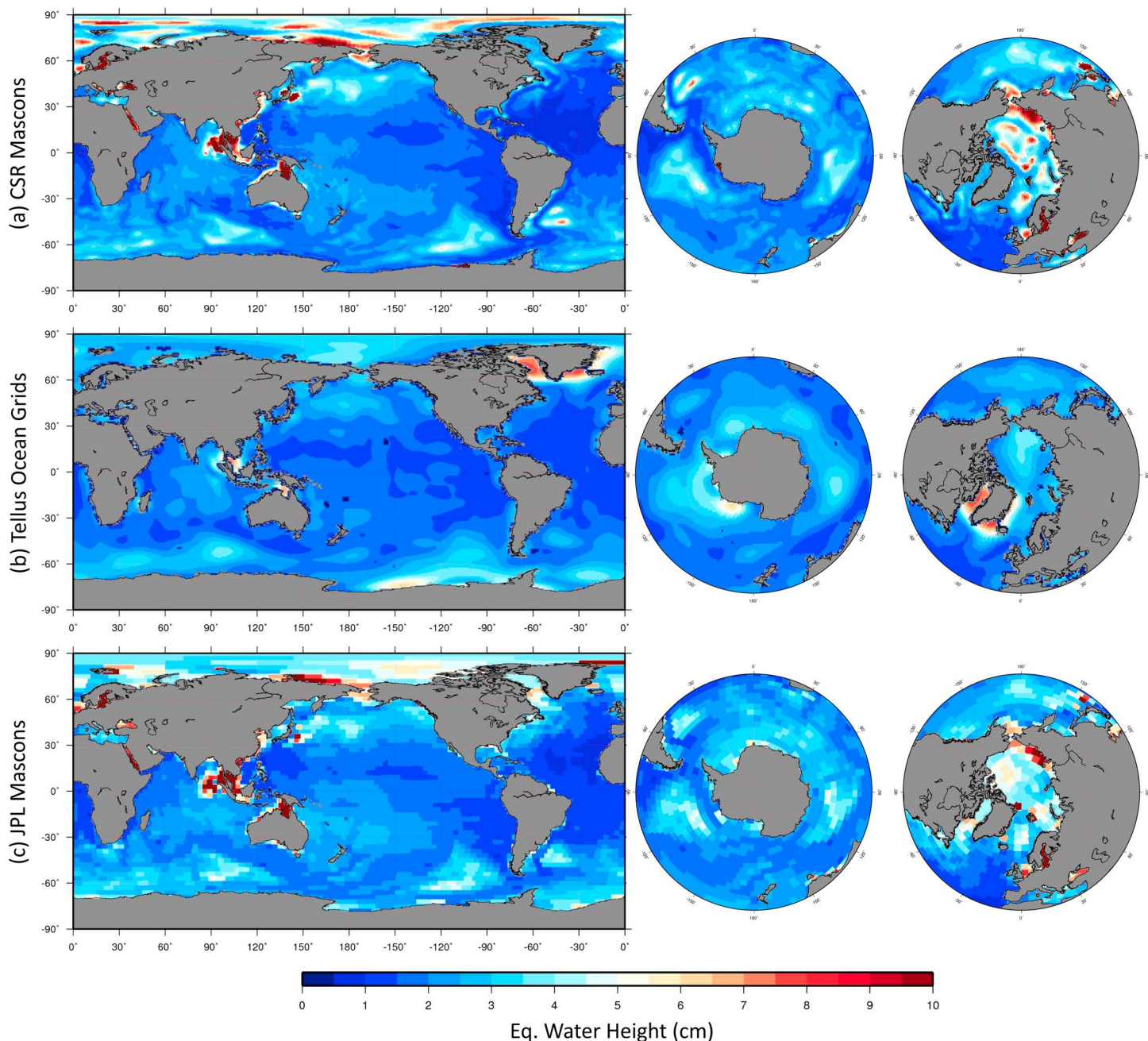


Figure 13. Standard deviation of the ocean bottom pressure from GRACE. (a) CSR Mascon solutions, (b) Tellus land grids, and (c) JPL Mascon solutions. CSR mascon solutions show higher-resolution signals in the Arctic and the Southern Ocean.

For OBP recorders in Arctic regions (Group D), CSR mascon solutions perform as well or better than the JPL mascon solutions with average correlation of 0.85 with the OBP recorder data, which is a significant improvement over the OMCT model which shows a correlation at 0.1. In the Kuroshio Extension region (Group E), the CSR mascon solutions perform better than JPL mascon solutions in all but two recorders. It should be noted that the nonmesoscale variability is well modeled in this region for OMCT which performs very well in correlations with the OBP recorder time series. The only region where the CSR mascons consistently underperform as compared to the JPL mascon solutions in the correlation comparison with the recorder data is in North Atlantic region near Svalbard (Group C). We think this is because of the way the land/ocean tiles are defined in this region for the CSR solution. JPL mascon solutions apply the Coastline Resolution Improvement (CRI) correction while the CSR mascons do not and is most likely the cause for the underperformance of the

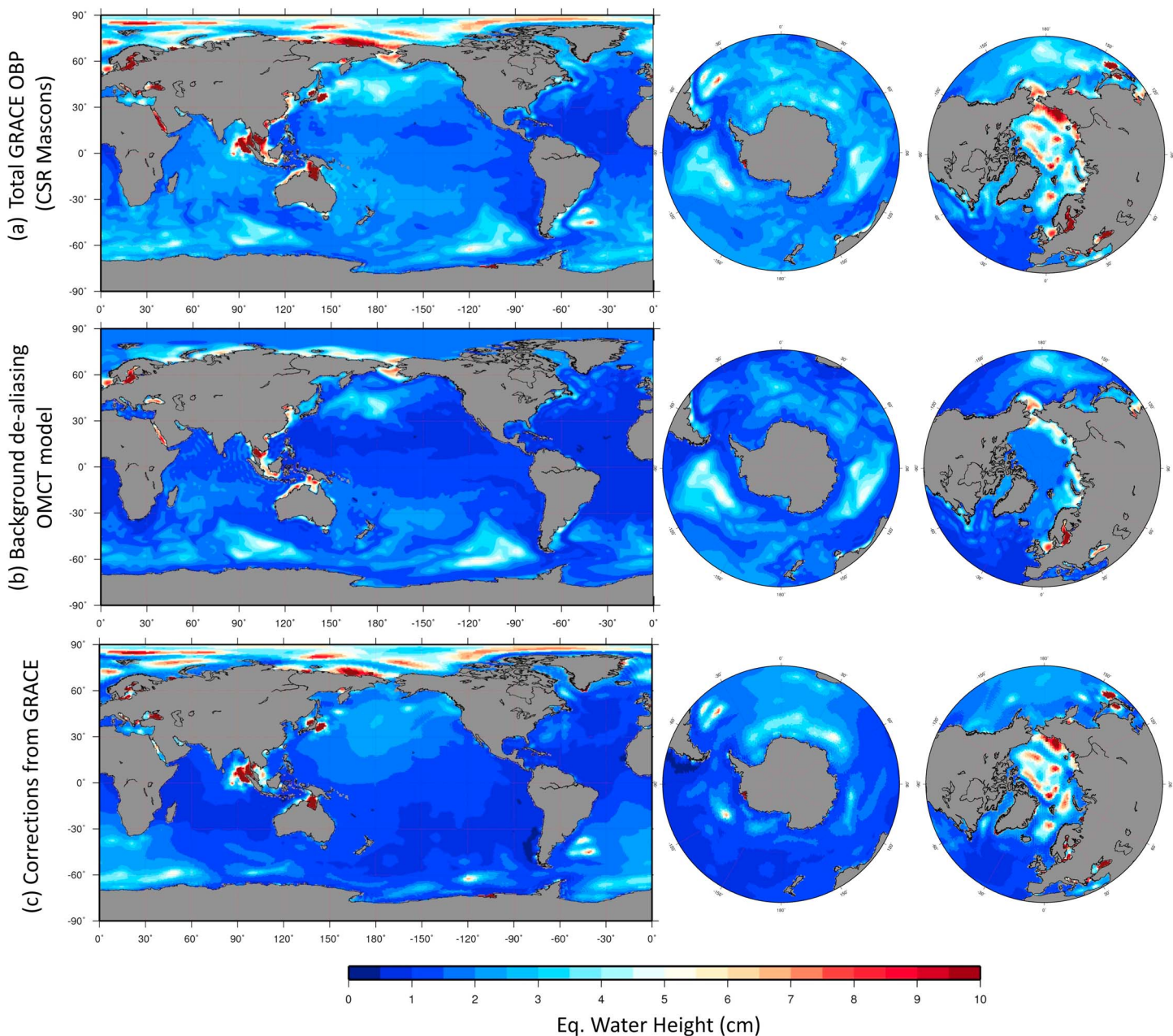


Figure 14. Standard deviation of the GRACE Ocean bottom pressure from CSR Mascons and corrections to OMCT. (a) Total OBP from CSR mascon solutions; (b) OBP from background de-aliasing model, OMCT; and (c) correction to OMCT from CSR GRACE mascon solutions.

CSR mascon solutions in this region with respect to the OBP recorders. It should be noted that the CSR mascon solutions still improves on the correlation of the background OMCT model with the recorder data in this region. The RMS of the difference with respect to the OBP recorder data is lower for the CSR mascon solutions except for all the recorders in Group C and three recorders in Group E where JPL mascons have lower error RMS as seen in Figure 17. The ocean bottom pressure standard deviation maps and the in situ data comparison demonstrates that the CSR mascon solutions provide a higher-resolution solution option for ocean studies.

6.5. Cryosphere

In this section we compare the ice loss estimates from the CSR mascon solutions and follow the same treatment of the solutions and studies as performed by *Watkins et al. [2015]*. As noted by *Watkins et al. [2015]* several different methods have been used to correct the stripe errors in the GRACE unconstrained

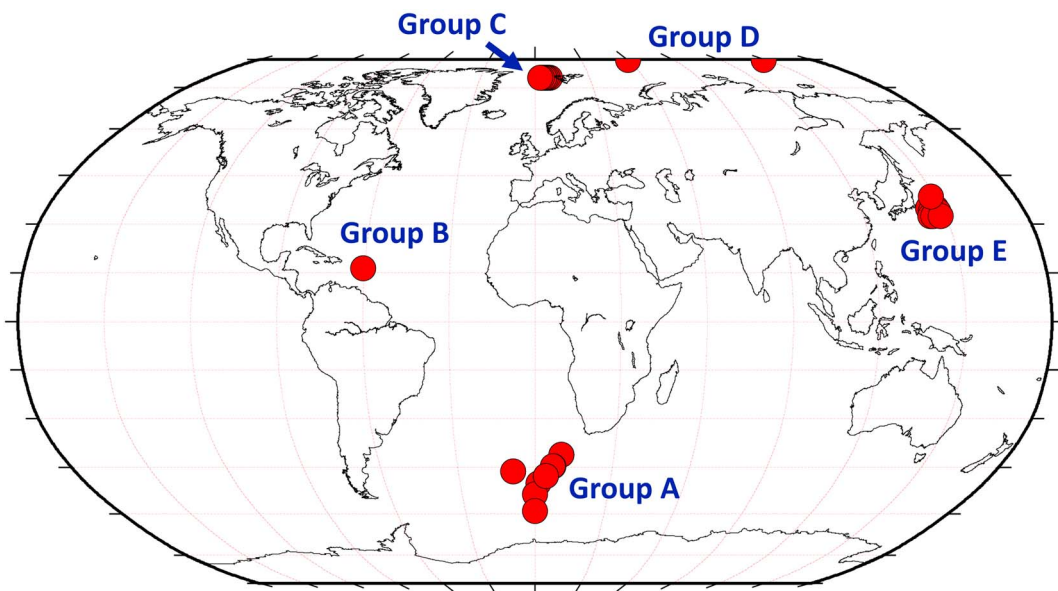


Figure 15. Locations of the 28 ocean bottom pressure recorders grouped into five groups used for comparison with the CSR mascon solutions.

spherical harmonic solutions. These methods include empirical orthogonal functions [Schrama and Wouters, 2011], scale factors with optimal averaging kernels [Velicogna, 2009], applying destriping filtering and Gaussian filtering [Baur et al., 2009], harmonics fits to regional forward models in Greenland [Chen et al., 2011], Wiener optimal filtering [Sasgen et al., 2012], and harmonic solution fits to regional mascons [Jacob et al., 2012]. The next generation mascon solutions from JPL [Watkins et al., 2015], GSFC Luthcke et al. [2013] and CSR provide a way to perform ice mass loss studies without having to utilize postprocessing techniques thus reducing the uncertainties associated with these processes.

Table 1 lists the same recent studies used by Watkins et al. [2015] and their published estimates for Greenland and Antarctica mass loss. We derive the estimate of ice mass loss from CSR mascon solutions for the same time spans as the published studies and include them to the comparison of the various mass loss estimates

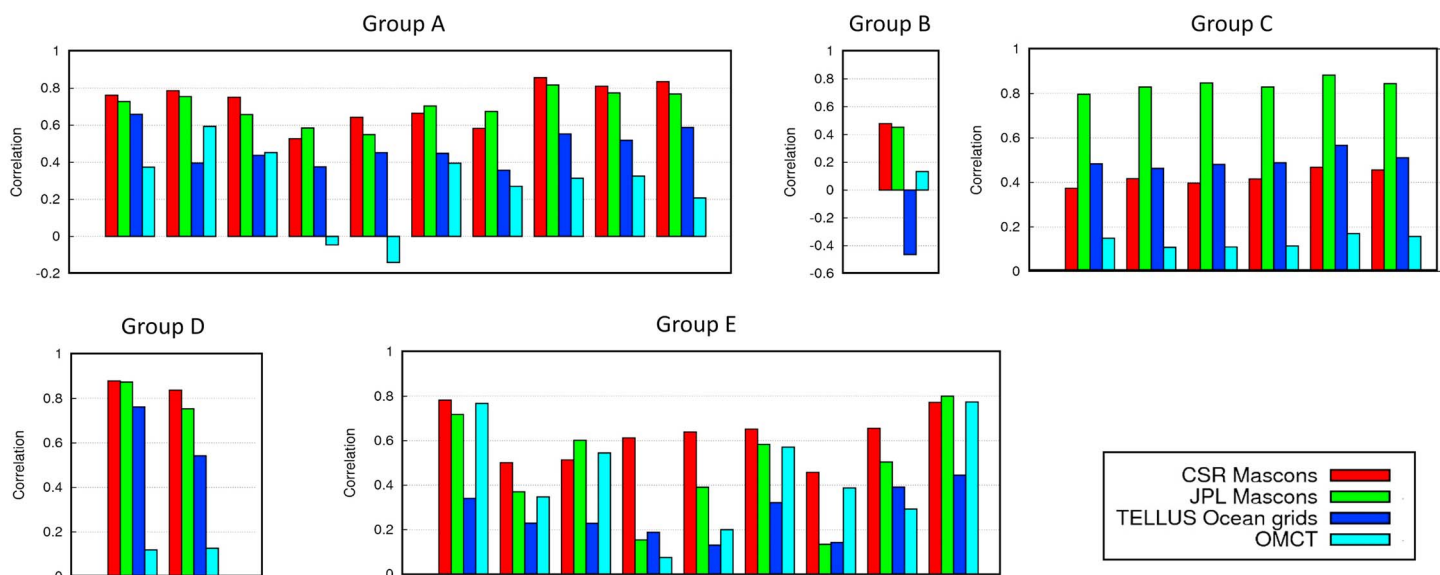


Figure 16. Correlations of four solutions/models with the data from 28 ocean bottom pressure recorder sites.

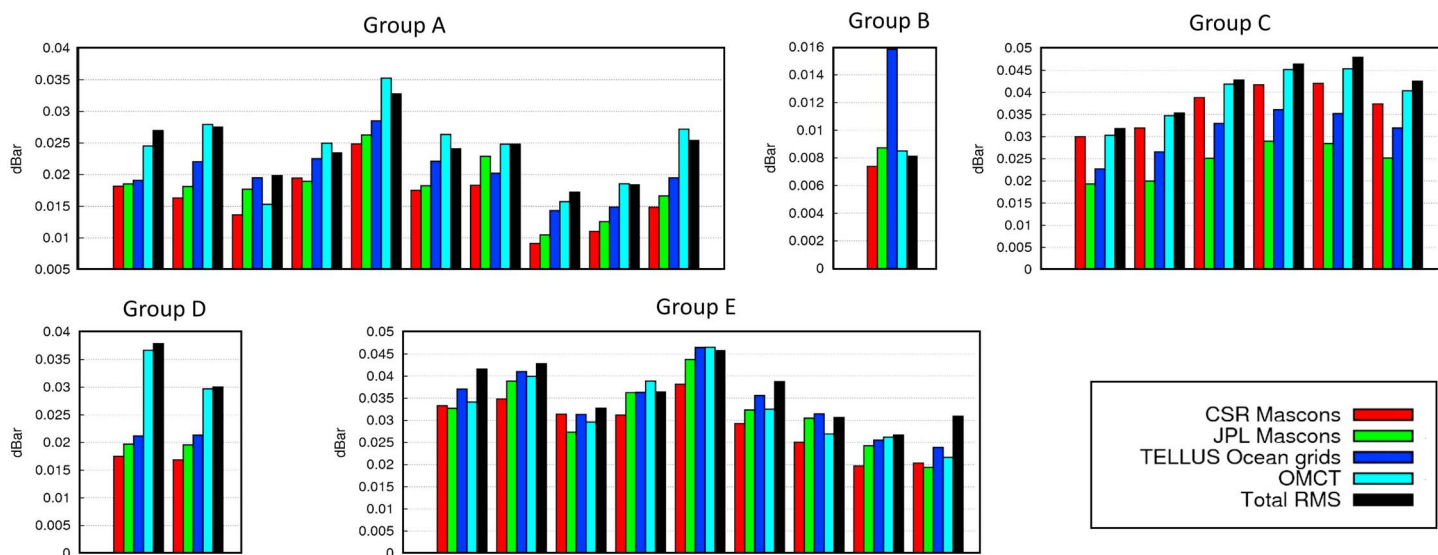


Figure 17. RMS of the difference of the four solutions/models with the data from 28 ocean bottom pressure recorder sites. Also included is the total signal RMS of the ocean bottom pressure recorder data for each site.

as published in *Watkins et al.* [2015]. We have used the same treatment of GIA for our ice loss estimate study as done by *Watkins et al.* [2015] in their study of ice mass loss. We apply the GIA correction for Greenland using ICE5G GIA model [*Geruo et al.*, 2013], but we do not include GIA correction for our ice loss estimates for Antarctica in order to compare the results published by *Watkins et al.* [2015]. Since we do not apply the land/ocean leakage correction like *Watkins et al.* [2015] we have to ensure that the regional kernel used to estimate the mass loss in the ice regions extends at least 120 km into the ocean. We define the tiles that include both land and the ocean are as land and doing this raises the possibility that the 120 km wide geodesic tile might be partly in the ocean, as seen in polar view maps of the geodesic tile distribution in Figure 1. The best way to account for this is to apply the coastline correction as applied by *Watkins et al.* [2015], but it does not impact CSR mascon solutions as much as it affects JPL mascon estimate due to the native estimation resolution of 1° for CSR mascons versus 3° for JPL mascons. Because of the high amplitude of the anomaly signal in the ice regions, the error associated in this case can be very high, and we recommend the 120 km extension to the basin when performing studies in the ice regions. For the studies in hydrology regions, the choice of the extended basin kernels should be made on a case-by-case basis.

Table 1 shows that the estimates of mass loss rates from the JPL mascon solutions are consistently higher than previously published results [*Watkins et al.*, 2015] and also consistently higher than the estimates from CSR mascon solutions. Table 1 also shows that the mass loss rates estimated for Greenland from CSR mascon solutions agree to within 5 Gt/yr with the estimates published by *Shepherd et al.* [2012], *Jacob et al.* [2012],

Table 1. Comparison of Published Trends for Greenland (Including GIA Correction) and Antarctica (Without GIA Correction) as Demonstrated in *Watkins et al.* [2015] With the Trends Calculated With CSR Mascons During the Same Time Frame

Study	Time Frame	Antarctica Trend (Gt/yr)			Greenland Trend (Gt/yr)		
		Study	CSR M	JPL M	Study	CSR M	JPL M
<i>Barletta et al.</i> [2013]	Jan 2003 to Nov 2011	-12 ± 36	-16 ± 24	-58 ± 21	-234 ± 20	-239 ± 30	-257 ± 29
<i>Jacob et al.</i> [2012]	Jan 2003 to Dec 2010	-23 ± 16	-05 ± 24	-54 ± 21	-222 ± 09	-227 ± 30	-244 ± 29
<i>Luthcke et al.</i> [2013]	Dec 2003 to Dec 2010	-34 ± 19	-09 ± 24	-67 ± 21	-230 ± 12	-234 ± 30	-249 ± 29
<i>Sasgen et al.</i> [2012]	Oct 2003 to Oct 2009	—	—	—	-238 ± 29	-218 ± 30	-235 ± 29
<i>Sasgen et al.</i> [2013]	Jan 2003 to Sep 2012	-61 ± 23	-23 ± 24	-56 ± 21	—	—	—
<i>Schrama et al.</i> [2014]	Feb 2003 to Jun 2013	-39 ± 18	-27 ± 24	-60 ± 21	-278 ± 19	-263 ± 30	-285 ± 29
<i>Shepherd et al.</i> [2012]	Jan 2003 to Dec 2010	-26 ± 30	-05 ± 24	-54 ± 21	-230 ± 27	-227 ± 30	-244 ± 29
<i>Velicogna and Wahr</i> [2013]	Jan 2003 to Nov 2012	-12 ± 35	-23 ± 24	-56 ± 21	-258 ± 41	-255 ± 30	-273 ± 29

Velicogna and Wahr [2013], *Barletta et al.* [2013], and *Luthcke et al.* [2013]. CSR mascon estimates comparison with other two Greenland studies by *Schrama et al.* [2014] and *Sasgen et al.* [2012] are within the formal uncertainty of the respective studies. The CSR mascons estimates of mass loss in Antarctica agrees to within 4 Gt/yr with *Barletta et al.* [2013]. For all the other studies the CSR estimates are within the formal uncertainties of the respective studies. The estimates of uncertainties for the ice loss estimates from Antarctic Ice Sheet (AIS) and Greenland from CSR mascons are not rigorously derived. They are derived the same way as derived in *Watkins et al.* [2015] by using the uncertainties provided by *Velicogna and Wahr* [2013]. *Velicogna and Wahr* [2013] estimate uncertainties due to each error source like atmosphere, oceans, filtering, and scaling after carefully consider all error sources. We use their uncertainty estimates for atmosphere, ocean circulation, glaciers/ice caps leakage, and hydrology leakage for AIS and Greenland in addition to GIA uncertainty for Greenland estimate.

6.6. Resolution

While these mascon solutions are estimated on geodesic grid tiles that are roughly 120 km wide, that is not the resolution of these GRACE mascon solutions. In order to determine a reasonable average resolution for the regularization filter used for these mascons, we define a filter matrix for the mascon regularization for each solution as described in section 5.3 of *Save et al.* [2012]. Similar to the procedure described in *Luthcke et al.* [2013], we can apply this filter matrix to a grid with 1.0 in the i th tile and 0.0 elsewhere, for all $i = 1, 40, 962$. Applying the filter matrix to this grid will result in a grid with nonzero values in more than just the i th tile. Multiple experiments have suggest that the summation of all the nonzero tiles within ~ 360 km to 480 km radius from the i th tile describes $\sim 100\%$ of the signal. This is roughly equivalent to a 200 km Gaussian spatial smoothing filter. This is consistent with the fact that the regularization constraint uses information from a 200 km Gaussian smoothed regularized spherical harmonic solutions from GRACE. While the regularization filter for the mascon solutions seem to have a resolution of 200 km, the resolution of these solution is still limited by the fundamental spatial resolution limitation of GRACE of roughly equivalent to 300 km radius Gaussian smoother. These solutions should be used only to perform basin-level time series analysis and never be used for time series analysis for a single grid point.

7. Summary

We have used the RL05 level 1b data to develop a new set of high-resolution global mascon solutions from GRACE. The solutions are developed on an equal-area geodesic grid of resolution of roughly 1° at the equator. The size of each mass element is roughly 120 km wide with an area of approximately 12,400 km 2 . These solutions are derived using only GRACE measurements and are not influenced by external geophysical models or data. Moreover, time variable regularization applied in this study ensures that future solutions are not influenced by measurements of past geophysical signals. We have replaced the C_{20} values in the mascon estimates with the estimates from SLR analysis [*Cheng and Tapley*, 2004], and the contribution of the geocenter has been corrected in accordance with the estimates from *Swenson et al.* [2008] to ensure consistency in the results obtained from different GRACE studies. The solutions meet the necessary condition that the postfit residuals do not indicate geospatial correlations, and all the signal is captured within the noise level of the GRACE level 1B measurements. The solutions show excellent correlation with the independent ocean bottom pressure recorder data. The solutions also show excellent agreement with the estimates of ice mass loss from multiple studies. The ice mass loss estimates from these solutions agree to within 5 Gt/yr with results from five out of seven studies in Greenland and to within 20 Gt/yr with results from five out of seven studies in Antarctica. Even though the solutions have been estimated in the equal-area geodesic grid domain, they will be resampled and released to the community as $0.5^\circ \times 0.5^\circ$ equiangular grid for the ease of analysis. The benefit of these mascon solutions is that the user no longer has to apply postprocessing to the GRACE spherical harmonic solutions or empirical scaling factors and can use these solutions as is for their applications. These solutions are global and not tailored toward a particular application, and hence, the solution set is applicable to all science areas of interest, e.g., oceanography, land surface hydrology, and cryosphere. While these mascon solutions are estimated on geodesic grid roughly 120 km wide, that is not the resolution of these GRACE solutions. These GRACE mascon solutions are limited by the band-limited nature of GRACE, with an approximate resolution of around 250–300 km near the equator. Rigorous uncertainty analysis for these solutions is ongoing and will be a topic of a follow-up publication. The CSR GRACE RL05 mascons solutions can be downloaded from the CSR GRACE webpage at <http://www.csr.utexas.edu/grace/>.

Acknowledgments

This research was sponsored under the NASA's GRACE contract NNL14AA00C. We sincerely thank the Texas Advanced Computing Center (TACC) for providing access to the high-performance computing resources without which this study was not possible. We thank Carmen Boening for providing the ocean bottom pressure recorder data for comparison with our solutions. GRACE Tellus land grids are available (<http://grace.jpl.nasa.gov>), supported by the NASA MEaSUREs Program. GRACE Tellus ocean grids were processed by Don P. Chambers, supported by the NASA MEaSUREs Program, and are available (<http://grace.jpl.nasa.gov>). GLDAS data were downloaded from <http://grace.jpl.nasa.gov>, which used the data from Goddard Earth Sciences Data and Information Services Center. The ECCO bottom pressure model data and the ICE5G GIA model was downloaded from <http://grace.jpl.nasa.gov>. The CSR GRACE RL05 mascons solutions can be downloaded from <http://www.csr.utexas.edu/grace/>. We thank the reviewers for their valuable comments and suggestions which led to an improvement of this manuscript.

References

- Barletta, V. R., L. S. Sørensen, and R. Forsberg (2013), Scatter of mass changes estimates at basin scale for Greenland and Antarctica, *Cryosphere*, 7(5), 1411–1432, doi:10.5194/tc-7-1411-2013.
- Baur, O., M. Kuhn, and W. Featherstone (2009), GRACE-derived ice-mass variations over greenland by accounting for leakage effects, *J. Geophys. Res.*, 114, B06407, doi:10.1029/2008JB006239.
- Böning, C., R. Timmermann, A. Macrander, and J. Schröter (2008), A pattern-filtering method for the determination of ocean bottom pressure anomalies from GRACE solutions, *Geophys. Res. Lett.*, 35, L18611, doi:10.1029/2008GL034974.
- Bruinsma, S., J.-M. Lemoine, R. Biancale, and N. Valès (2010), CNES/GRGS 10-day gravity field models (release 2) and their evaluation, *Adv. Space Res.*, 45(4), 587–601, doi:10.1016/j.asr.2009.10.012.
- Chambers, D. P. (2006), Observing seasonal steric sea level variations with GRACE and satellite altimetry, *J. Geophys. Res.*, 111, C03010, doi:10.1029/2005JC002914.
- Chambers, D. P. (2012), *GRACE Monthly Ocean Mass Grids NetCDF Release 5.0. Ver. 5.0.*, PO.DAAC, California, doi:10.5067/TEOCN-0N005. [Available at <http://grace.jpl.nasa.gov>, accessed on 2015-01-04.]
- Chambers, D. P., and J. Bonin (2012), Evaluation of release-05 GRACE time-variable gravity coefficients over the ocean, *Ocean Sci.*, 8(5), 859–868, doi:10.5194/os-8-859-2012.
- Chambers, D. P., and J. K. Willis (2010), A global evaluation of ocean bottom pressure from GRACE, OMCT, and steric-corrected altimetry, *J. Atmos. Ocean. Technol.*, 27(8), 1395–1402, doi:10.1175/2010JTECH0738.1.
- Chen, J., C. Wilson, and B. Tapley (2011), Interannual variability of Greenland ice losses from satellite gravimetry, *J. Geophys. Res.*, 116, B07406, doi:10.1029/2010JB007789.
- Cheng, M., and B. D. Tapley (2004), Variations in the Earth's oblateness during the past 28 years, *J. Geophys. Res.*, 109, B09402, doi:10.1029/2004JB003028.
- Famiglietti, J., M. Lo, S. Ho, J. Bethune, K. Anderson, T. Syed, S. Swenson, C. de Linage, and M. Rodell (2011), Satellites measure recent rates of groundwater depletion in California's Central Valley, *Geophys. Res. Lett.*, 38, L03403, doi:10.1029/2010GL046442.
- Flechtner, F. (2007), *Aod1b Product Description Document for Product Releases 01 to 04 (Rev. 3.1, April 13, 2007)*, pp. 327–750, GRACE Project Document. [Available at ftp://podaac.jpl.nasa.gov/allData/grace/docs/AOD1B_PDD_v4.4.pdf.]
- Fukumori, I. (2002), A partitioned Kalman filter and smoother, *Mon. Weather Rev.*, 130(5), 1370–1383, doi:10.1175/1520-0493(2002)130<1370:AKF&S>1.0.CO;2.
- Geruo, A., J. Wahr, and S. Zhong (2013), Computations of the viscoelastic response of a 3-D compressible earth to surface loading: An application to glacial isostatic adjustment in Antarctica and Canada, *Geophys. J. Int.*, 192(2), 557–572, doi:10.1093/gji/ggs030.
- Jacob, T., J. Wahr, W. T. Pfeffer, and S. Swenson (2012), Recent contributions of glaciers and ice caps to sea level rise, *Nature*, 482(7386), 514–518, doi:10.1038/nature10847.
- Kanzow, T., F. Flechtner, A. Chave, R. Schmidt, P. Schwintzer, and U. Send (2005), Seasonal variation of ocean bottom pressure derived from Gravity Recovery and Climate Experiment (GRACE): Local validation and global patterns, *J. Geophys. Res.*, 110, C09001, doi:10.1029/2004JC002772.
- Kim, S.-B., T. Lee, and I. Fukumori (2007), Mechanisms controlling the interannual variation of mixed layer temperature averaged over the Niño-3 region, *J. Clim.*, 20(15), 3822–3843, doi:10.1175/JCLI4206.1.
- Landerer, F., and S. Swenson (2012), Accuracy of scaled GRACE terrestrial water storage estimates, *Water Resour. Res.*, 48, W04531, doi:10.1029/2011WR011453.
- Laven, K. V. (2010), Gridsphere Code. [Available at <https://www.mathworks.com/matlabcentral/fileexchange/28842-grid-sphere>.]
- Lemoine, J.-M., S. Bruinsma, S. Loyer, R. Biancale, J.-C. Marty, F. Perosanz, and G. Balmino (2007), Temporal gravity field models inferred from GRACE data, *Adv. Space Res.*, 39(10), 1620–1629, doi:10.1016/j.asr.2007.03.062.
- Long, D., B. R. Scanlon, L. Longuevergne, A. Y. Sun, D. N. Fernando, and H. Save (2013), GRACE satellite monitoring of large depletion in water storage in response to the 2011 drought in Texas, *Geophys. Res. Lett.*, 40, 3395–3401, doi:10.1002/grl.50655.
- Luthcke, S. B., H. Zwally, W. Abdalati, D. Rowlands, R. Ray, R. Nerem, F. Lemoine, J. McCarthy, and D. Chinn (2006), Recent Greenland ice mass loss by drainage system from satellite gravity observations, *Science*, 314(5803), 1286–1289, doi:10.1126/science.1130776.
- Luthcke, S. B., A. A. Arendt, D. D. Rowlands, J. J. McCarthy, and C. F. Larsen (2008), Recent glacier mass changes in the Gulf of Alaska region from GRACE mascon solutions, *J. Glaciol.*, 54(188), 767–777.
- Luthcke, S. B., T. Sabaka, B. Loomis, A. Arendt, J. McCarthy, and J. Camp (2013), Antarctica, Greenland and Gulf of Alaska land-ice evolution from an iterated GRACE global mascon solution, *J. Glaciol.*, 59(216), 613–631, doi:10.3189/2013JoG12J147.
- Macrander, A., C. Böning, O. Boebel, and J. Schröter (2010), Validation of GRACE gravity fields by in-situ data of ocean bottom pressure, in *System Earth via Geodetic-Geophysical Space Techniques*, pp. 169–185, Springer, Berlin, doi:10.1007/978-3-642-10228-8_14.
- Mayer-Gürr, T. (2007), ITG-Grace03s: The latest GRACE gravity field solution computed in Bonn, presented at the Joint International GSTM and SPP Symposium, Potsdam, Germany, 15–17 Oct.
- Peralta-Ferriz, C., J. H. Morison, J. M. Wallace, J. A. Bonin, and J. Zhang (2014), Arctic ocean circulation patterns revealed by GRACE, *J. Clim.*, 27(4), 1445–1468.
- Ringler, T. D., and D. A. Randall (2002), A potential enstrophy and energy conserving numerical scheme for solution of the shallow-water equations on a geodesic grid, *Mon. Weather Rev.*, 130(5), 1397–1410, doi:10.1175/1520-0493(2002)130<1397:APEC>2.0.CO;2.
- Rodell, M., et al. (2004), The global land data assimilation system, *Bull. Am. Meteorol. Soc.*, 85(3), 381–394.
- Rodell, M., I. Velicogna, and J. S. Famiglietti (2009), Satellite-based estimates of groundwater depletion in India, *Nature*, 460(7258), 999–1002, doi:10.1038/nature08238.
- Rowlands, D., S. Luthcke, J. McCarthy, S. Klosko, D. Chinn, F. Lemoine, J.-P. Boy, and T. Sabaka (2010), Global mass flux solutions from GRACE: A comparison of parameter estimation strategies—Mass concentrations versus Stokes coefficients, *J. Geophys. Res.*, 115, B01403, doi:10.1029/2009JB006546.
- Sabaka, T., D. Rowlands, S. Luthcke, and J.-P. Boy (2010), Improving global mass flux solutions from Gravity Recovery and Climate Experiment (GRACE) through forward modeling and continuous time correlation, *J. Geophys. Res.*, 115, B11403, doi:10.1029/2010JB007533.
- Sasgen, I., M. van den Broeke, J. L. Bamber, E. Rignot, L. S. Sørensen, B. Wouters, Z. Martinec, I. Velicogna, and S. B. Simonsen (2012), Timing and origin of recent regional ice-mass loss in greenland, *Earth Planet. Sci. Lett.*, 333, 293–303, doi:10.1016/j.epsl.2012.03.033.
- Sasgen, I., et al. (2013), Antarctic ice-mass balance 2003 to 2012: Regional reanalysis of GRACE satellite gravimetry measurements with improved estimate of glacial-isostatic adjustment based on GPS uplift rates, *Cryosphere*, 7, 1499–1512, doi:10.5194/tc-7-1499-2013.
- Save, H., and S. Bettadpur (2013), Using Tikhonov regularization for spatial projections from CSR regularized spherical harmonic GRACE solutions, Abstract G32A-06 presented at 2013 Fall Meeting, AGU, San Francisco, Calif., 9–13 Dec.
- Save, H., S. Bettadpur, and B. D. Tapley (2012), Reducing errors in the GRACE gravity solutions using regularization, *J. Geod.*, 86(9), 695–711, doi:10.1007/s00190-012-0548-5.

- Save, H. V. (2009), Using regularization for error reduction in GRACE gravity estimation, PhD thesis, Univ. of Texas at Austin.
[Available at <https://repositories.lib.utexas.edu/handle/2152/7665>.]
- Scanlon, B. R., Z. Zhang, R. C. Reedy, D. R. Pool, H. Save, D. Long, J. Chen, D. M. Wolock, B. D. Conway, and D. Winester (2015), Hydrologic implications of GRACE satellite data in the Colorado River Basin, *Water Resour. Res.*, *51*, 9891–9903, doi:10.1002/2015WR018090.
- Schrama, E. J., and B. Wouters (2011), Revisiting Greenland ice sheet mass loss observed by GRACE, *J. Geophys. Res.*, *116*, B02407, doi:10.1029/2009JB006847.
- Schrama, E. J., B. Wouters, and R. Rietbroek (2014), A mascon approach to assess ice sheet and glacier mass balances and their uncertainties from GRACE data, *J. Geophys. Res. Solid Earth*, *119*, 6048–6066, doi:10.1002/2013JB010923.
- Shepherd, A., et al. (2012), A reconciled estimate of ice-sheet mass balance, *Science*, *338*(6111), 1183–1189, doi:10.1126/science.1228102.
- Swenson, S., and J. Wahr (2006), Post-processing removal of correlated errors in GRACE data, *Geophys. Res. Lett.*, *33*, L08402, doi:10.1029/2005GL025285.
- Swenson, S., D. Chambers, and J. Wahr (2008), Estimating geocenter variations from a combination of GRACE and ocean model output, *J. Geophys. Res.*, *113*, B08410, doi:10.1029/2007JB005338.
- Swenson, S. C. (2012), GRACE monthly land water mass grids NetCDF release 5.0. ver. 5.0.PO.DAAC, California, doi:10.5067/TELND-NC005.
[Available at <http://grace.jpl.nasa.gov/>, accessed on 2015-01-04.]
- Tapley, B., B. Schutz, and G. H. Born (2004a), *Statistical Orbit Determination*, Academic Press. [Available at <http://store.elsevier.com/Statistical-Orbit-Determination/Bob-Schutz/isbn-9780126836301/>.]
- Tapley, B. D., S. Bettadpur, M. Watkins, and C. Reigber (2004b), The gravity recovery and climate experiment: Mission overview and early results, *Geophys. Res. Lett.*, *31*, L09607, doi:10.1029/2004GL019920.
- Tapley, B. D., S. Bettadpur, J. C. Ries, P. F. Thompson, and M. M. Watkins (2004c), GRACE measurements of mass variability in the Earth system, *Science*, *305*(5683), 503–505, doi:10.1126/science.1099192.
- Thomas, J. (1999), An analysis of gravity-field estimation based on intersatellite dual-1-way biased ranging, *Tech. Rep.* [Available at ftp://podaac.jpl.nasa.gov/allData/grace/docs/JPL_PUB_98-15.pdf.]
- Tiwari, V., J. Wahr, and S. Swenson (2009), Dwindling groundwater resources in Northern India, from satellite gravity observations, *Geophys. Res. Lett.*, *36*, L18401, doi:10.1029/2009GL039401.
- Velicogna, I. (2009), Increasing rates of ice mass loss from the Greenland and Antarctic ice sheets revealed by GRACE, *Geophys. Res. Lett.*, *36*, L19503, doi:10.1029/2009GL040222.
- Velicogna, I., and J. Wahr (2013), Time-variable gravity observations of ice sheet mass balance: Precision and limitations of the GRACE satellite data, *Geophys. Res. Lett.*, *40*, 3055–3063, doi:10.1002/grl.50527.
- Velicogna, I., T. Sutterley, and M. Van den Broeke (2014), Regional acceleration in ice mass loss from Greenland and Antarctica using GRACE time-variable gravity data, *Geophys. Res. Lett.*, *41*, 8130–8137, doi:10.1002/2014GL061052.
- Wahr, J., M. Molenaar, and F. Bryan (1998), Time variability of the Earth's gravity field: Hydrological and oceanic effects and their possible detection using GRACE, *J. Geophys. Res.*, *103*(B12), 30,205–30,229, doi:10.1029/98JB02844.
- Watkins, M. M., D. N. Wiese, D.-N. Yuan, C. Boening, and F. W. Landerer (2015), Improved methods for observing Earth's time variable mass distribution with GRACE using spherical cap mascons, *J. Geophys. Res. Solid Earth*, *120*, 2648–2671, doi:10.1002/2014JB011547.
- Wiese, D. N. (2015), GRACE monthly global water mass grids NetCDF release 5.0. ver. 5.0, PO.DAAC, Calif., doi:10.5067/TEMSC-OCL05.
[Available <http://grace.jpl.nasa.gov/>, accessed on 2015-01-04.]